Materials Advances

ROYAL SOCIETY OF CHEMISTRY

PERSPECTIVE

View Article Online
View Journal | View Issue

Cite this: *Mater. Adv.*, 2026, 7, 4474

Strategies for vat photopolymerization additive manufacturing of metals and ceramics

Jie Zeng [a] and Max A. Saccone *[b]

Vat photopolymerization (VP) additive manufacturing (AM) enables the fabrication of complex 3D metal and ceramic objects by using light to selectively cure liquid resins, followed by post-processing to convert precursors to inorganic materials. This technique has been applied across diverse practical applications and can produce metals and ceramics with unique and tailored properties. In this perspective, we discuss VP-based AM within the broader context of the AM field, with a focus on the recent advances in fabrication of metals and ceramics, including approaches where precursors are incorporated prior to printing and those where they are introduced post-printing. We also evaluate polymer thermal decomposition processes, a critical step in VP-based AM of metals and ceramics. Finally, we discuss current challenges, future opportunities, and emerging technological directions including multi-material printing and high-entropy alloy manufacturing.

Received 4th February 2026,
Accepted 20th April 2026

DOI: 10.1039/d6ma00166a

rsc.li/materials-advances

1. Introduction

1.1 Overview of metal additive manufacturing

Additive manufacturing (AM), also known as 3D printing, is a technique in which a computer aided design (CAD) file is processed layer-by-layer to manufacture various customized products, such as metals, ceramics, polymers and composites.[1–3] AM can fabricate complex geometries with customized properties without the need for assembly, which otherwise could not be made using conventional manufacturing methods. Furthermore, AM offers additional advantages such as high material utilization, low-cost rapid prototyping, a simplified supply chain for efficient low-volume production, and often lower fixed costs relative to conventional manufacturing approaches.[4] AM processes are classified into seven broad categories based on the feedstock format and the energy source:[5] powder bed fusion (PBF), directed energy deposition (DED), binder jetting (BJ), material extrusion (ME), material jetting (MJ), sheet lamination (SL), and vat polymerization (VP). An in-depth discussion of these processes can be found in a textbook written by Gibson *et al.*[6]

Metal AM has been widely adopted in various industries including aerospace,[7] automobile,[8] medical[9] and construction.[10] PBF, DED, and BJ are the most commonly used technologies for metal AM due to their ability to produce metallic parts with higher mechanical performance than those processes that use wires or metallic sheets as feedstock materials, and they have received extensive investigation.[11,12] Commonly processed materials include titanium alloys, aluminum alloys, nickel-based alloys, high entropy alloys, and steels, among others. However, these powder-based methods have challenges when fabricating materials with high thermal conductivity due to difficulties in maintaining a localized melting zone, and a propensity for high porosity and thermal distortions, typically requiring intensive optimization of processing parameters.[13] These limitations have motivated growing interest in indirect metal AM strategies that decouple geometric definition from metal densification by leveraging polymeric intermediates or scaffolds.

Vat photopolymerization combined with post-processing conversion reactions is a promising example of such an indirect approach, enabling the fabrication of 3D metallic and ceramic structures by using printed polymer parts as scaffolds for subsequent materials processing. VP offers the advantages of high dimensional resolution, precision, and speed, making it a powerful tool for fabricating high-quality, complex inorganic structures. VP has been extensively studied for fabrication of polymeric materials and has seen wide applications in recent years. According to an independent market report, the VP photopolymer market reached a size of $3.14 billion in 2024 and is expected to grow at a compound annual growth rate of 11.3% from 2025 to 2033.[14] While this market is mainly dedicated to fabrication of polymeric parts and is dominated by dental applications, which accounted for 32.38% of the market share in 2024, there is an opportunity to expand the capabilities of VP printing more broadly to inorganic materials.[14] However, several challenges remain, including the need for high precursor loadings that lead to excessive resin viscosity, limited precursor-resin compatibility that can

[a] *Department of Chemical and Biological Engineering, University of Colorado Boulder, Boulder, CO 80303, USA*
[b] *Paul M. Rady Department of Mechanical Engineering, University of Colorado Boulder, Boulder, CO 80309, USA. E-mail: max.saccone@colorado.edu*

compromise printability, and complex post-processing steps that influence the final structural and mechanical properties. Here, we discuss recent progress towards addressing these challenges in VP-based metal AM to support continued development in this field and to identify areas with opportunities for future impactful research.

1.2 Overview of vat photopolymerization

Depending on the light source and polymerization mechanism, VP technologies can be classified into different categories including scanning stereolithography (SLA), digital light processing (DLP), two-photon lithography (TPL), and volumetric additive manufacturing (VAM).

Scanning stereolithography (SLA) was the first commercially available AM system introduced to the market in 1980s.[15] It operates using either the ''top-down'' or ''bottom-up'' approach combined with a point-to-point tracing strategy, as shown schematically in Fig. 1A. Since SLA techniques expose one voxel at a time, they make use of high-intensity laser spots but require high linear translation speeds to achieve efficient throughput. In contrast, digital light processing (DLP), uses a digital micromirror device (DMD) or a liquid crystal display (LCD) as a dynamic mask to project sequential 2D sliced images within a vat to fully cure the entire resin layer at a time, shown schematically in Fig. 1B. Compared to SLA techniques, DLP techniques tend to expose each voxel with a lower intensity, but for a longer duration. Continuous liquid interface production (CLIP) is a variation of DLP printing, projecting a sequence of 2D images through an oxygen-permeable, UV-transparent window below a liquid resin bath to continuously fabricate a 3D object,[16] shown schematically in Fig. 1C. The continuous nature of CLIP enables faster fabrication (exceeding 50 cm h^{-1}) with smoother surface finishes. Two-photon lithography (TPL) is the most common and well-developed multiphoton lithography (MPL), in which the local photopolymerization of photoresins can be carried out by absorption of two photons stimulated by focused and pulsed femtosecond laser radiation, shown schematically in Fig. 1D. TPL allows for the fabrication of structures with feature sizes as small as 65 nm, and even reaching 9 nm when a secondary inhibition laser is employed.[17–19] Volumetric additive manufacturing (VAM) techniques (Fig. 1E) create a 3D light intensity distribution that enables polymerization and crosslinking to occur in a controlled, contactless manner within the volume of a liquid photoresin, leading to the formation of the desired object.[20,21] VAM techniques enable the use of highly viscous resins and the fabrication of centimeter-scale geometries within tens of seconds, significantly faster than traditional layer-by-layer 3D printing methods.

Understanding the polymerization chemistries involved in VP printing enables modifications to printing parameters such as UV wavelength, exposure time, and printing speed to optimize the final product. In typical free-radical VP systems, photoresins consist of monomers/oligomers (30–99+ wt%), photoinitiators (less than 5 wt%), and UV blockers (less than 0.5 wt%), with representative molecules illustrated in Fig. 2. Monomers/oligomers generally contain one or more functional groups that can participate in the polymerization reaction, with (meth)acrylate-based and thiol–ene-based chemistries being the most commonly used.[23] Monofunctional monomers often serve as reactive diluents to reduce resin viscosity, whereas multifunctional oligomers can lead to increased viscosity and crosslinking. Photoinitiators play an important role in the photopolymerization reaction, as they undergo a series of complex physical or chemical changes during the initiation process.[23] In free-radical photopolymerizations, photoinitiators that undergo homolytic bond cleavage to generate free radicals are known as Norrish type I initiators, such as benzil ketals and acyl phosphine oxides.[24] Photoinitiators that undergo photoexcitation and then

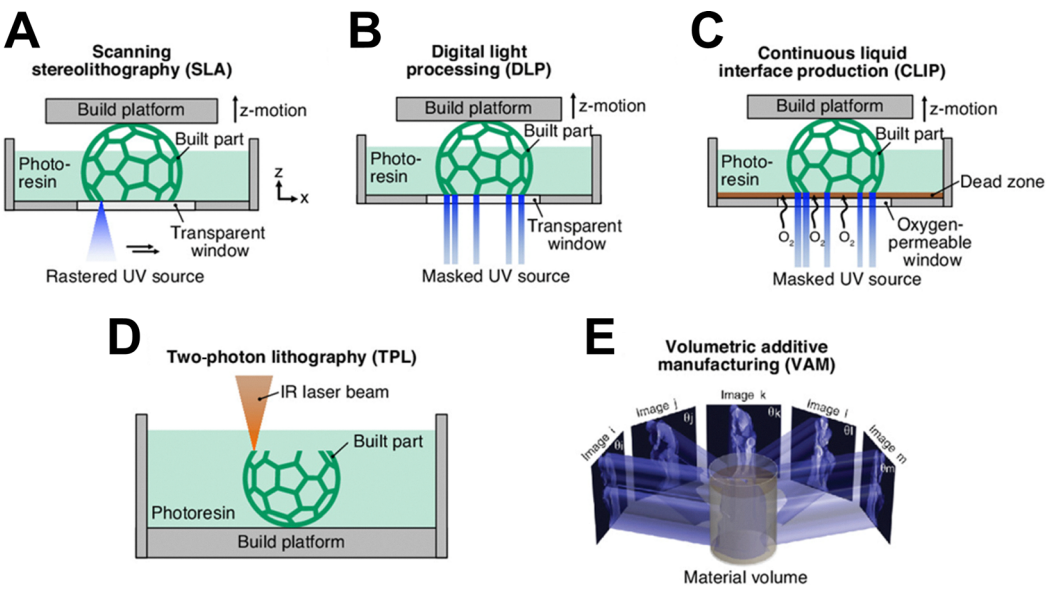

Fig. 1 Schematics of common VP techniques including (A) scanning stereolithography, (B) digital light processing, (C) continuous liquid interface production, (D) two-photon lithography, and (E) volumetric additive manufacturing. Adapted from ref. 20 and 22 with permission.

abstract hydrogen or electrons from co-initiator species (*e.g.*, tertiary amines) to produce radicals are classified as Norrish type II initiators, with benzophenones and thioxanthones being common examples.[25] UV blockers, such as tartrazine, are incorporated

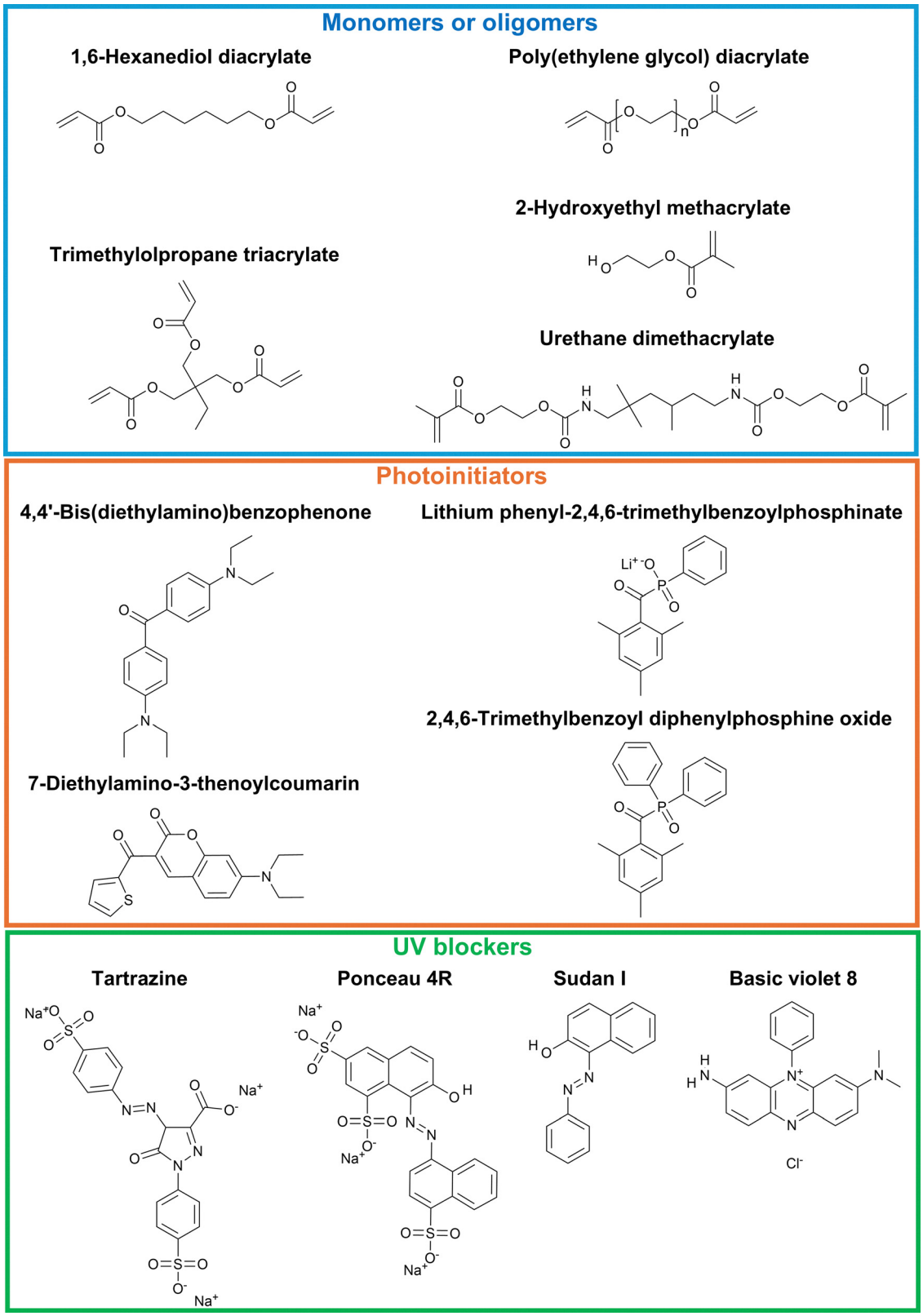

Fig. 2 Molecular structures of representative components used in VP-based photoresins.

to regulate light penetration depth by attenuating incident radiation and quenching propagating radicals.[26] This enables precise control over curing depth and prevents premature gelation of resins. Beyond free-radical systems, cationic polymerization is an alternative polymerization method that is widely used and well-studied in VP processes. It typically involves cations generated from the decomposition of onium or diazonium salts, which react with monomers *via* ring-opening reactions, leading to chain-growth through ion pair propagation.[27]

2. VP preparation methods for metals and ceramics

Vat photopolymerization techniques fundamentally enable fabrication of polymeric materials. To use VP methods to prepare metals and ceramics, these materials or their precursors must be introduced into the processing chain, either before, during, or after the printing step.

2.1 Precursors introduced prior to printing

In VP-based AM of inorganic materials, one of the most widely adopted strategies for fabricating metal or ceramic components involves incorporating functional precursors directly into the photoresin before printing. This category includes both heterogeneous resins, such as particle-loaded slurries, and homogeneous resins, where metal salts or organometallics are molecularly dispersed within the photopolymer matrix, or where inorganic precursors comprise the polymer chain.

2.1.1 Heterogeneous resins. Dispersing metal or ceramic powders, typically with particle sizes ranging from 0.05 μm to 10 μm, in a liquid photoresin is a common VP-based approach for fabricating metals and ceramics.[28] This heterogeneous resin is patterned to form a composite polymer structure, often referred to as a ''green body''. The green body is then thermally treated in an appropriate atmosphere to remove the organic matrix and yield the desired metal or ceramic structure. To improve the structural integrity of the final printed metal product during post-processing, a high filler content, typically larger than 40 vol%, is necessary to ensure stable thermal decomposition.[29] However, incorporating particles into the resin inevitably increases resin viscosity and can lead to the formation of a jammed suspension upon shearing, which reduces the printing speed due to the increased Stefan adhesion and requires the use of mechanical recoating tools (*e.g.*, blades or wipers) to spread and level the resin during printing.[30] Also, particle agglomeration and setting can cause inhomogeneous distribution of particles in the vat, resulting in non-uniform curing and inconsistent material properties in the printed parts. Another drawback of heterogeneous resin techniques is that dispersed particles can cause light scattering, which reduces the cure depth and limits the resolution achievable by lithography techniques compared to that of conventional transparent photoresins.[31] In general, smaller particle sizes and higher solid loadings increase viscosity and light scattering, thereby reducing printing resolution, although they improve densification and structural integrity of the fabricated parts. While the use of optically transparent particles can help mitigate scattering effects, increased viscosity remains a fundamental challenge.

To mitigate the challenges related to increased viscosity, and particle agglomeration and setting, dispersants or surfactants are commonly used to minimize particle interactions and improve suspension stability. In general, ceramic particles typically possess a high density of surface hydroxyl groups, rendering them hydrophilic and prone to agglomeration due to the strong interparticle interactions.[32] In contrast, most UV-curable resins used in VP are non-aqueous and hydrophobic. By adding dispersants with hydrophobic anchoring head groups and hydrophilic end chains, the surfaces of ceramic particles can be converted from hydrophilic to hydrophobic.[33] For metal particles, the surfaces are usually covered by thin oxide layers, which exhibit a lower hydroxyl group density and stronger van der Waals attractions compared to ceramic particles. Consequently, stabilization of metal particles in VP resins relies on dispersants that exhibit strong affinity toward oxide-covered metallic surfaces while maintaining compatibility with the photopolymer matrix. Such surface modification results in the formation of a core–shell structure that provides steric hindrance and/or enhanced electrostatic repulsion, thereby ensuring homogeneous dispersion of particles within the suspension. Commonly used dispersants for metal/ceramic particles include stearic acid (SA),[29,34] oleic acid (OA),[29,35] Disperbyk (BYK),[36,37] and silane coupling agent KH560.[34] An optimal dispersant concentration can substantially enhance the rheological properties of slurries, resulting in lower viscosity, reduced sedimentation rates, and improved dispersion stability.[38] In addition to mitigating interparticle interactions, dispersants also influence the photopolymerization behavior of the slurry. Studies have shown that as the absorption coefficient of dispersants increases, the light transmittance of the slurry decreases significantly.[39] Fig. 3 shows a typical VP-based heterogeneous resin method with ceramic particles coated with dispersant molecules. Its SEM results show that the fabricated Al_2O_3 ceramic structures with controllable micro-sized features could be printed by using different dispersants.

Table 1 compares the target material, VP technique, resin composition including photoinitiators (PIs) and metal precursors (MPs), resin viscosity at different shear rate (SR), relative density, mechanical properties, and feature dimensions of the final printed objects of recently reported heterogeneous resin methods employing various dispersants. Here, the relative density is defined as the ratio of the measured bulk density to the theoretical density of corresponding material, in which bulk density is typically determined using the Archimedes method. As summarized in Table 1, VP-based heterogeneous resin methods can achieve near-full densification in ceramic systems, but this generally requires high solid loadings accompanied by high resin viscosities, typically greater than the low-viscosity range of 0.1–1 Pa s and up to approximately 35 Pa s.[40] When high densification is achieved, the resulting mechanical properties approach bulk values.[41,42] Such highly loaded

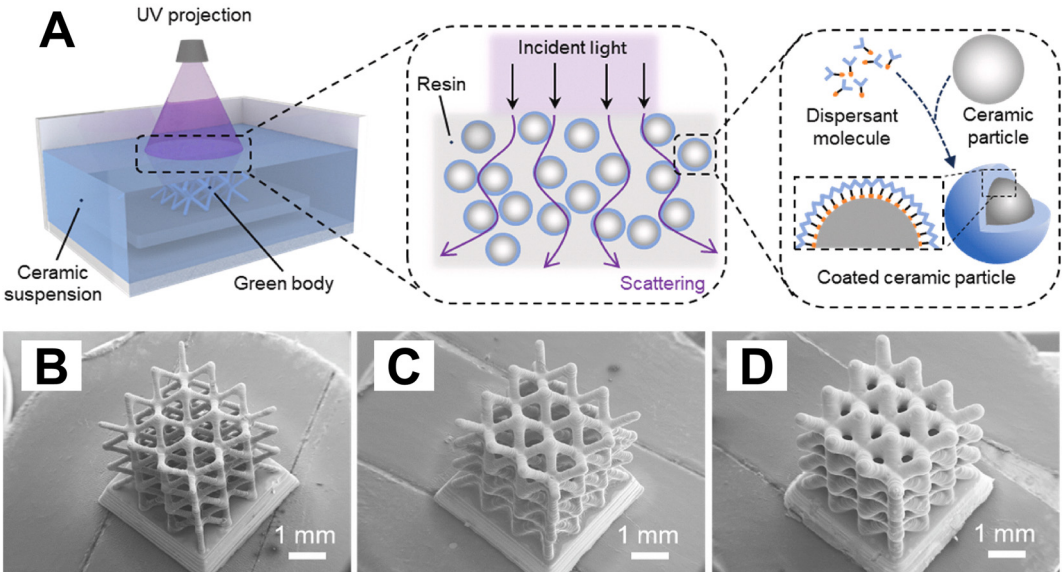

Fig. 3 (A) Schematic illustrations of a VP-based heterogeneous resin method, showing the propagation of incident light within the suspension and ceramic particles coated with dispersant molecules. (B)–(D) SEM images of Al_2O_3 ceramic green bodies 3D printed with different dispersants. (B) Containing KOS110. (C) Containing BYK111. (D) Containing BYK180. Adapted from ref. 39 with permission.

systems exhibit large and anisotropic linear shrinkage, commonly around 19–26% in *X*–*Y* plane and about 21–28% along the *Z* direction, with extreme cases reported in copper-based systems showing *Z*-direction shrinkage of up to 63%.

2.1.2 Homogeneous resins. To address the challenges associated with heterogeneous resins, such as particle agglomeration and setting, and light scattering during the photocuring process, many studies have reported the development of particle-free metal-precursor-containing homogeneous resins. These photoresins typically consist of metal ions dispersed within a polymer matrix or metal heteroatoms incorporated into the polymer backbone.[49,50] The ability to design and control homogeneous resins with well-defined compositions and functionalities is critical to tailoring their properties for VP-based metal AM.

Various metal precursors can be incorporated into homogeneous resins either as inorganic salts (*e.g.*, nitrates, chlorides, acetates) or as organometallic compounds (*e.g.*, acetylacetonates, alkoxides, amino complexes). Metal salts are an inexpensive precursor that can achieve high metal content and favorable rheological properties when dissolved in aqueous solution. However, they are generally difficult to dissolve in organic polymers, and typically require a hydrophilic polymer scaffold. The development of metal-ion-rich, water-based binder matrices, such as acrylate-based hydrogels is well-established. In this system, metal ions are effectively entrapped and homogeneously distributed within the polymeric network. For example, Luitz *et al.* demonstrated the preparation of a platinum-containing organic–inorganic photoresin by dissolving K_2PtCl_4 in polyethylene glycol diacrylate and the water-soluble monomer Genomer 7311.[51] By replacing the metal precursor with $Na_6(H_2W_{12}O_{40})$, they also fabricated tungsten ion photoresin for the tungsten and tungsten carbide manufacturing.[52] Similarly, Cai *et al.* formulated a water-based photoresin containing $(NH_4)_6[H_2W_{12}O_{40}]\cdot xH_2O$ as the tungsten source, $Ni(NO_3)_2\cdot 6H_2O$ as a sintering aid, acrylic acid-2-hydroxyethyl as an active diluent, polyethylene glycol diacrylate as a cross-linker.[53] Yee *et al.* reported a method involving the dissolution of zinc nitrate hexahydrate in water, followed by mixing with polyethylene glycol diacrylate and a two-photon initiator, 7-diethylamino-3-thenoylcourmarin, to produce a homogeneous zinc-ion photoresin for two-photon lithography.[49] Beyond this work, Yee *et al.* further developed a DLP printing route using lithium and cobalt nitrate containing hydrogels to fabricate lithium cobalt oxide architectures, one of the most widely used cathode materials for lithium-ion batteries, shown in Fig. 4A.[54] In general, these studies demonstrate that water-based, metal-ion-containing hydrogel systems provide a versatile platform for achieving homogeneous precursor distribution.

Another approach to fabricate homogeneous photoresins for metal AM involves the use of organic metal precursors. These precursors may directly react with the polymer, often leading to cross-linking, or be incorporated *via* complexation to ensure bonding of the metal to the polymer backbone. For instance, Vyatskikh *et al.* reported a ligand exchange reaction between nickel alkoxide and acrylic acid to synthesize nickel acrylate, which was subsequently combined with pentaerythritol triacrylate and a photoinitiator (7-diethylamino-3-thenoylcoumarin) to form a nickel-ion-containing homogeneous photoresin.[55] The resulting metal-containing polymer structures were then pyrolyzed to remove the organic components and convert the polymer into metallic nickel. Using complexing agents to incorporate metals into polysiloxane matrices for the fabrication of metal doped, polymer-derived ceramic is another key

Table 1 Comparison of reported VP-based heterogeneous resin methods for metal AM

Target material	VP technique	Resin composition	Resin viscosity and shear rate (SR)	Relative density	Mechanical properties	Feature dimensions	Ref.
Alumina	DLP	**Monomers/oligomers:** 1,6-hexanediol diacrylate, ethoxylated pentaerythritol tetraacrylate, di-functional aliphatic polyurethane acrylate **MPs:** yttria-coated alumina (79 wt%) **Dispersants:** oleic acid (1.0 wt%), BYK9077	1.97 Pa s **SR:** 13 s^{-1}	97.53%	**Flexural strength:** 455.37 ± 32.17 MPa **Weibull modulus:** 16.88	Not reported	35
Alumina	DLP	**Monomers/oligomers:** 1,6-hexanediol diacrylate, trimethylolpropane triacrylate **PIs:** 2,4,6-trimethylbenzoyldiphenyl phosphine **MPs:** alumina (40 vol%) **Dispersants:** BYK-180 (5 wt%)	71 mPa s **SR:** 80 s^{-1}	Not reported	Not reported	**Beam diameter:** 115 μm	39
Alumina	DLP	**Monomers/oligomers:** 1,6-hexanediol diacrylate, trimethylolpropane triacrylate **PIs:** phenylbis(2,4,6-trimethylbenzoyl)phosphine oxide **MPs:** alumina (50 vol%) **Dispersants:** BYK111 (3 wt%)	1.09 Pa s **SR:** 25 s^{-1}	Not reported	Not reported	**Shrinkage:** X–Y = 19.8%, Z = 20.9%	43
Aluminum alloy	DLP	**Monomers/oligomers:** 1,6 hexanediol diacrylate, trimethylolpropane triacrylate, **PIs:** 2,4,6-trimethylbenzoyl diphenylphosphine oxide **Inhibitors:** *tert*-butylhydroquinone **MPs:** AA5052 aluminum alloy powder (55 vol%) **Dispersants:** SP-710 (5 wt%)	34.7 Pa s **SR:** 10 s^{-1}	91.23%	**Elastic modulus:** 63.886 GPa, **Vickers hardness:** 1.82 GPa	**Feature resolution:** 0.9 mm	44
Zirconia	DLP	**Monomers/oligomers:** urethane dimethacrylate, hydroxyethyl methacrylate, acryloyl morpholine **MPs:** yttria-stabilized zirconia (40 vol%) **PIs:** CPI01 **Dispersants:** CPD01 and CPD09 (3 wt%)	3.8 Pa s **SR:** 30 s^{-1}	98.3%	**Flexural strength:** 708 MPa **Vickers hardness:** 14.7 GPa **Fracture toughness:** 5.49 MPa $m^{1/2}$	**Shrinkage:** X–Y = 21.6%, Z = 27.8%	45
Zirconia	SLA	**Monomers/oligomers:** 1,6-hexanediol diacrylate, trimethylolpropane triacrylate **PIs:** diphenyl(2,4,6- trimethylbenzoyl)phosphine oxide **MPs:** zirconia (40 vol%) **Dispersants:** BYK-103 (5 wt%)	1.03 Pa s **SR:** 65 s^{-1}	99%	**Vickers hardness:** 14 GPa	Not reported	46
Zirconia	DLP	**Monomers/oligomers:** acrylate-based resin AnyCubic **MPs:** yttria-stabilized zirconia (30 vol%) **Dispersants:** BYK-103 (10 wt%)	0.93 Pa s **SR:** 10 s^{-1}	98.2 ± 0.3%	**Vickers hardness:** 12.89 GPa	**Shrinkage:** X–Y = 25.7%, Z = 27.1%	37
Copper	CLIP	**Monomers/oligomers:** 1,6-hexanediol diacrylate, trimethylolpropane ethoxylate triacrylate **PIs:** Omnirad 819 **MPs:** copper sulfate (50 wt%) **Dispersants:** BYK-2013 (7 wt%)	0.16 Pa s **SR:** 80 s^{-1}	Not reported	Not reported	**Feature resolution:** 50–100 μm **Shrinkage:** X–Y = 58%, Z = 63%	36
Copper	CLIP	**Monomers/oligomers:** 1,6-hexanediol diacrylate, trimethylolpropane ethoxylate triacrylate **PIs:** Omnirad 819 **MPs:** copper sulfate (62 wt%) **Dispersants:** Triton X-100	0.41 Pa s **SR:** 25 s^{-1}	Not reported	Not reported	**Shrinkage:** 59%	47
WC–Co hardmetals	SLA	**Monomers/oligomers:** trimethylolpropane triacrylate, hexamethylene diacrylate **PIs:** diphenyl(2,4,6-trimethylbenzoyl)phosphine oxide **MPs:** WC and Co (40 vol%) **Dispersants:** TEGO DISPERS 655 (2 wt%)	1.58 Pa s **SR:** 100 s^{-1}	99.5%	**Rockwell hardness:** 86.9 HRA **Surface roughness:** 2.26 μm	Not reported	48

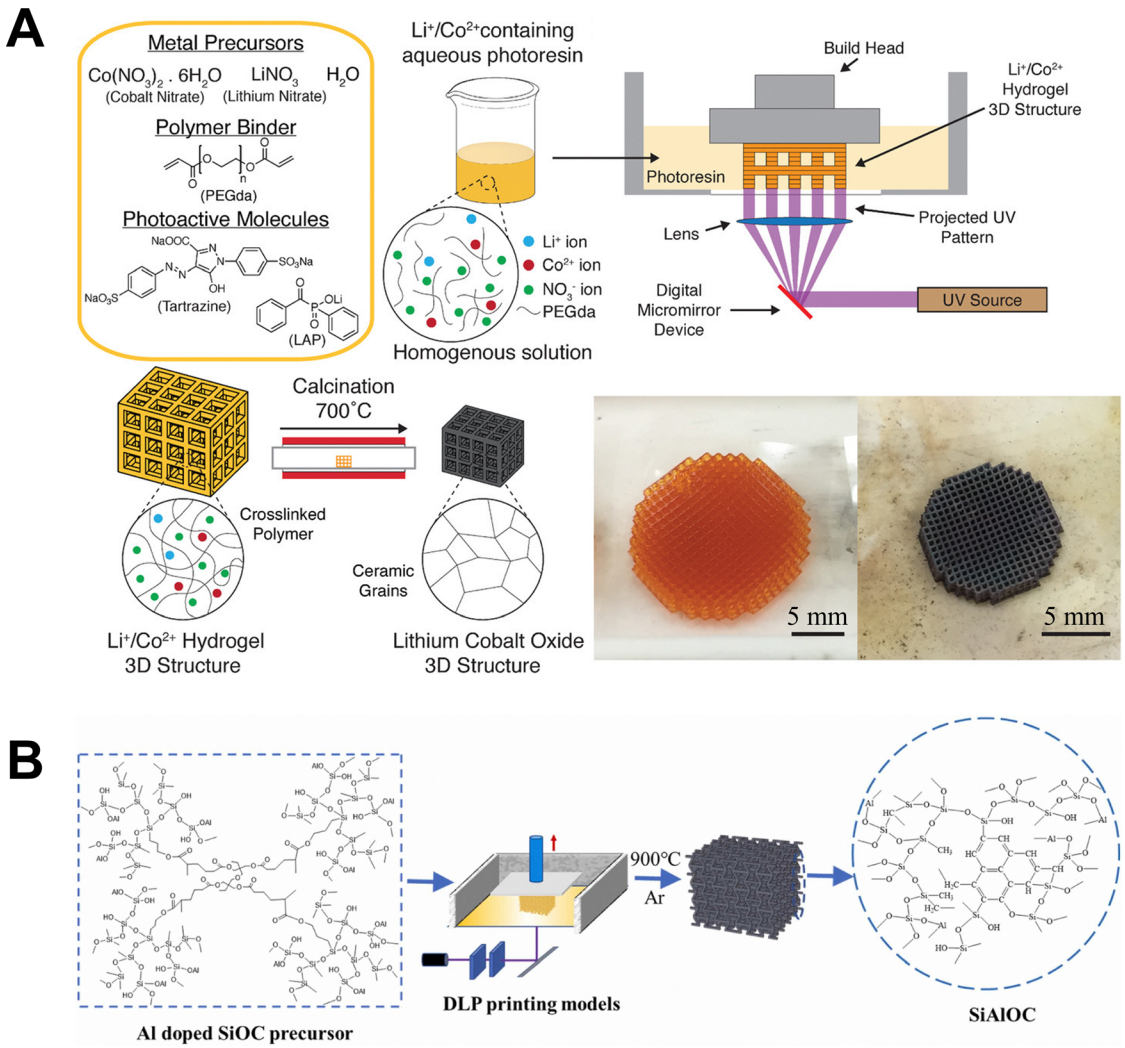

Fig. 4 Schematic illustrations of VP-based homogeneous resin methods for metal AM. (A) Resin formulation and schematic of DLP printing of a Li^+/Co^{2+} hydrogel 3D structure. The printed Li^+/Co^{2+} hydrogel (left optical image) is then calcined to form a self-similar LCO structure (right optical image). (B) SiAlOC precursor solution molecular structure and schematic of DLP printing of SiAlOC. Adapted from ref. 54 and 58 with permission.

application of this approach, as illustrated in Fig. 4B. Fu *et al.* demonstrated the fabrication of multiple metal doped polymer-derived SiOC ceramics by using methacrylic acid to incorporate Zr and Ti into methyl-silsesquioxane photoresin through a complexation reaction.[56] Similarly, Essmeister *et al.* reported the development of polymer-derived Ni/SiOC materials with catalytic activity in CO_2 methanation, using methacrylic acid to incorporate Ni into methyl-silsesquioxane photoresin.[57] Hu *et al.* formulated an Al-doped SiOC photoresin by combining methyl-silsesquioxane resin with aluminum acetylacetonate as the raw material.[58] Overall, these approaches demonstrate that molecular-level incorporation of metal species into polymer backbones offers enhanced control over composition.

Table 2 compares the target material, VP technique, resin composition, product composition, chemical and mechanical properties, and feature dimensions of recently reported VP-based homogeneous resin methods. As summarized in Table 2, homogeneous resin methods enable molecular-scale metal ion distribution and can achieve excellent printing resolution (250–400 nm), particularly when hydrophilic, metal ion-rich polymer matrices are combined with TPL technique. However, these advantages are often accompanied with extreme linear shrinkage (40–80%) and limited bulk densification. Approaches based on organic metal precursor can partially mitigate shrinkage (35–41%) but typically operate at low metal contents (below 5 wt%) and yield only modest mechanical strength. Notably, VP-based homogeneous resin methods target highly diverse end applications-including micro-mechanical metamaterials, electronics, and catalysis, leading to substantial variation in product compositions, architectures, and testing protocols. Consequently, reported chemical and mechanical properties span a wide range, which makes direct cross-comparison between studies inherently difficult.

The use of homogeneous resins effectively addresses the viscosity challenges caused by high particle loadings and reduces light scattering compared to heterogeneous resins. However, a

Table 2 Comparison of reported VP-based homogeneous resin methods for metal AM

Target material	VP technique	Resin composition	Product composition	Chemical/mechanical properties	Feature dimensions	Ref.
Zinc oxide	TPL	**Monomers/oligomers:** poly(ethylene glycol) diacrylate **PIs:** 7-diethylamino-3-thenoylcoumarin **MPs:** zinc nitrate hexahydrate (~51 wt%)	**Zn:** 45.0 at% **O:** 48.9 at%	**Loading stiffness:** 2.37 ± 0.15 kN m^{-1} **Unloading stiffness:** 2.52 ± 0.13 kN m^{-1} **Failure compressive strain:** 3.5%	**Feature resolution:** 250 nm **Shrinkage:** 87 ± 2%	49
Platinum	TPL	**Monomers/oligomers:** polyethylene glycol diacrylate, Genomer 7311 **PIs:** 4,4′-bis(diethylamino)-benzophenone **MPs:** potassium tetrachloroplatinate (25 wt%)	**Pt:** 96.8 wt%	**Conductivity:** 6.32 × 10^6 S m^{-1} **Surface roughness:** 0.3 nm	**Feature resolution:** 330 nm **Shrinkage:** 80.8%	51
Tungsten, tungsten carbide	TPL	**Monomers/oligomers:** polyethylene glycol diacrylate, Genomer 7311 **PIs:** 4,4′-bis(diethylamino)-benzophenone **MPs:** sodium metatungstate (33 wt% for tungsten and 47 wt% for tungsten carbide)	**W:** 93 at% **WC:** 45 at% tungsten	**WC indentation hardness:** 64.9 ± 11.1 MPa **WC modulus:** 1.314 ± 0.295 GPa. **Surface roughness:** W: 214 nm, WC = 162 nm **Compressive strength (strut breaking):** W: 0.9 MPa, WC: 5.1 MPa	**Beam diameter:** W: 8.9 ± 0.1 μm, WC: 6.9 ± 0.2 μm **Shrinkage:** W: 53.4%, WC: 52.7%	52
Tungsten	DLP	**Monomers/oligomers:** polyethylene glycol diacrylate **PIs:** PEG-BAPO **UV blocker:** tartrazine **MPs:** ammonium metatungstate (47.8 wt%)	**W:** 95.31 wt%	**Micropillar compressive strength:** 1552 MPa **Nanoindentation hardness:** 7.5 GPa **Overall compressive strength:** 13 MPa **Surface roughness:** 2.86 μm	**Feature resolution:** 35 μm **Shrinkage:** ~40%	53
Nickel	TPL	**Monomers/oligomers:** acrylic acid, pentaerythritol triacrylate **PIs:** 7-diethylamino-3-thenoylcoumarin **MPs:** nickel 2-methoxyethoxide	**Ni:** 91.8 wt%	**Specific strength:** 2.1–7.2 MPa g^{-1} cm^3 **Structural stiffness:** ~47–174 MPa **Compressive strength (at first buckling):** 6.9–18.2 MPa	**Beam diameter:** 300–400 nm **Shrinkage:** ~80%	55
Zr/Ti/SiOC	DLP	**Monomers/oligomers:** methyl-silsesquioxane, 3-(trimethoxysilyl)-propyl methacrylate **PIs:** phenylbis(2,4,6-trimethylbenzoyl)phosphine oxide **MPs:** zirconium *n*-propoxide, titanium isopropoxide **Complexing agents:** methacrylic acid	**Zr:** 1.84 wt% **Ti:** 0.33 wt%	**Compression strength:** 0.124 MPa **Hardness:** 7.61 GPa	**Shrinkage:** 35.4%	56
Ni/SiOC	Masked-SLA	**Monomers/oligomers:** methyl-silsesquioxane, 3-(trimethoxysilyl)-propyl methacrylate, tri (propyleneglycol)-methyl ether **PIs:** phenylbis(2,4,6-trimethylbenzoyl)phosphine oxide **MPs:** nickel(II) nitrate hexahydrate **Complexing agents:** methacrylic acid	**Ni:** 5 wt%	**CO_2 methanation:** 25.6% CO_2 conversion and 53.4% CH_4 selectivity at 400 °C	**Feature resolution:** 400 μm	57
Al/SiOC	DLP	**Monomers/oligomers:** methyl-silsesquioxane, 3-methacryloxypropyltrimethoxy, trimethylolpropane triacrylate **PIs:** phenylbis(2,4,6-trimethylbenzoyl)phosphine oxide **MPs:** aluminum acetylacetonate	**Al:** 0.51 wt%.	**Compression strength:** 12.76 MPa **Champion piezoresistivity:** 75.44% **Gauge factor:** −647.49	**Shrinkage:** 41%	58

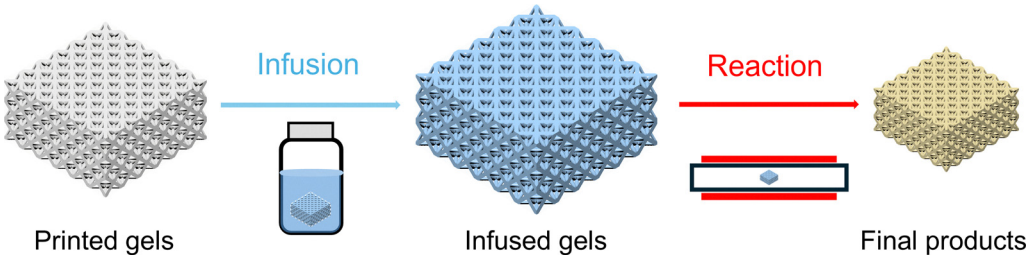

Fig. 5 Schematic of infusion-reaction methods. Precursors are introduced into a printed scaffold (gel) during an infusion step after printing, then undergo a reaction to form final products.

major drawback of this approach is that these photoresins are often not commercially available, due to the diverse chemical properties of metal ions and the need for a complex multi-step synthesis. Developing resins with both high metal content and appropriate optical properties remains a significant challenge, as the maximum loading of metal precursors is constrained by a combination of precursor solubility, molecular compatibility, viscosity, and photopolymerization kinetics. Moreover, the specific requirements of the polymerization process narrow the range of compatible polymeric materials, as certain metal precursors (*e.g.*, Cu^{2+}) can inhibit polymerization, making compositional tuning more challenging due to their interactions with the curing chemistry.[59] In particular, transition metal ions could introduce additional light absorption through ligand-to-metal charge transfer, reducing light penetration depth, while also acting as radical scavengers that increase the critical exposure dose.[60] These effects are generally less pronounced than those introduced by dedicated UV blockers (*e.g.*, tartrazine), but still require quantitative evaluation and re-optimization of printing parameters, such as exposure dose and layer thickness to ensure reliable printing performance.

2.2 Precursors introduced in post-printing

Unlike heterogeneous or homogeneous resin-based approaches that require the incorporation of metals into photoresins prior to printing, infusion-reaction methods introduce metal precursors after printing, thereby reducing the complexity associated with resin formulation and printing parameter optimization, shown schematically in Fig. 5. These approaches offer distinct advantages in kinetic control by decoupling the material's solid-state transformation from the geometric definition of the printed architecture, presenting a promising route for the fabrication of metal and ceramic micro/nano architectures.

2.2.1 Hydrogel infusion additive manufacturing. Hydrogel infusion additive manufacturing (HIAM) is a simple and versatile metal AM technique based on infusion-reaction methods. Developed by Saccone & Gallivan *et al.* in 2022, HIAM enables the fabrication of various metals (*e.g.*, copper, nickel, tungsten, and high-entropy alloys) from a single photoresin, without the need for pre-loading metal precursors, as shown schematically in Fig. 6.[61] The process involves first printing organogels (which is typically composed of poly(ethylene glycol) diacrylate (PEGda)) into the desired 3D shapes, followed by a solvent exchange step that converts the organogels into hydrogels. These hydrogel scaffolds are then infused with metal precursor solutions, calcined and reduced to yield corresponding metal replicas. This novel approach to metal structure fabrication enables quick iteration, compositional tuning, parallelization and multimaterial integration, offering significant advantages in spatial resolution and geometric complexity. For example,

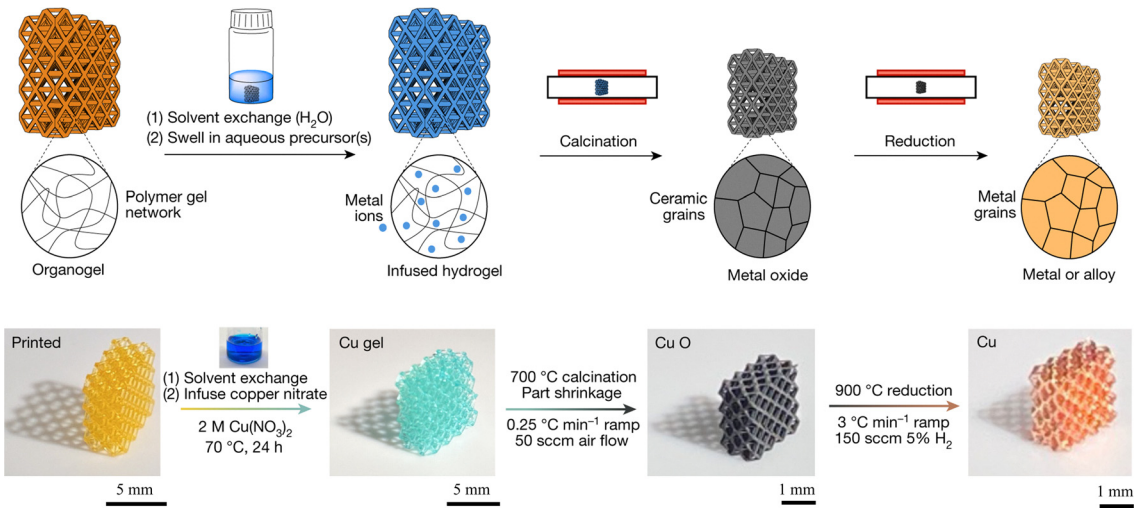

Fig. 6 Schematic of HIAM process and optical images of the HIAM process for Cu metal. Adapted from ref. 61 with permission.

printing copper at the sub-millimeter scale is particularly challenging using conventional laser-based sintering techniques due to its high thermal conductivity.[62] HIAM overcomes this limitation and enables the fabrication of copper structures with feature sizes below 50 μm.

Nanoindentation experiments performed on HIAM-derived Cu and $Cu_{55}Ni_{45}$ revealed hardness values of 1.81 ± 0.37 GPa and 2.15 ± 0.22 GPa, respectively.[61] To investigate the mechanisms underlying this enhanced hardness in HIAM-derived alloys, Tran *et al.* recently conducted a systematic study on the reduction processes and microstructural evolution of the HIAM-derived Cu_xNi_{1-x} alloy system.[63] Their findings indicated substantial growth of metallic nuclei into microscale grains during reduction, which facilitated the formation of low energy interfaces and numerous annealing twins. These microstructural features entrapped unreduced oxide grains, resulting in hierarchical nanocomposite structures that contributed to hardness values up to four times greater than those of bulk annealed Cu_xNi_{1-x}. Uniaxial compression experiments on both Cu-rich and near-equiatomic micropillars further revealed composition-dependent nanomechanical behaviors. The primary sources of defects were likely to be internal pores formed by H_2O generation during reduction and dispersed unreduced oxides resulting from incomplete reduction. The extent and distribution of these defects varied with alloy composition, influencing the density of inclusions and voids in the final material. These microstructural heterogeneities likely played a significant role in the elevated nanoindentation hardness observed in HIAM-derived alloys.

Within the HIAM processes, the solvent-exchange step is essential to remove residual organic solvent in the structure, which can lead to formation of porosity upon calcination and reduction. The presence of organic solvent can also cause precipitation of the metal salt during the swelling process, leading to an inhomogeneous distribution of the metal precursors. An investigation of the impact of both inorganic and organic precursors on the final printed structures was conducted by Yaw *et al.*[64] The study demonstrates that the concentration of hydrogel formulations and the choice of inorganic salts with different decomposition events can significantly influence the resulting morphology and porosity of the printed structures.

However, the exact mechanisms of metal ion diffusion within hydrogels remain unclear due to the highly disordered nature of polymer chains, the high concentration of metal ions in solution, and the large excess of water molecules.[64] From a thermodynamic perspective, diffusion in hydrogels is generally entropy-driven and governed by gradients in Gibbs free energy or chemical potential, which dictate the direction of mass transport.[65] Ion diffusion mechanisms can be classified into three main types: physical adsorption, chemical adsorption, and ion exchange.[66] The dominant metal ion adsorption mechanism varies significantly depending on the type of metal ion, the ionic composition of the solution, and the surface properties of the hydrogel. In the HIAM process, physical adsorption plays a role, in which metal ions are loosely bound to the hydrogel *via* weak forces such as electrostatic attractions. Electrostatic attractions occur between oppositely charged metal ions and functionalized hydrogels. Functional groups such as carboxyl, hydroxyl, amide, and amine play a crucial role in inducing surface charge and mediating ion adsorption.[66] The strength of electrostatic interactions depends heavily on the surface charge density of the hydrogel, which is governed by the ionization of these groups, a pH-dependent process. Electrostatic interactions also influence the solubility of solutes within the hydrogel.[65] For instance, hydrophilic solutes with polar groups can form hydrogen bonds with the matrix, increasing retention and reducing diffusion rates.

Table 3 compares the target material, VP technique, resin composition, product composition, mechanical properties, and feature dimensions of recently reported VP-based HIAM and HIAM-variant methods. As summarized in Table 3, HIAM and its variants combine infusion-reaction strategies to achieve high metal content (around 85–95 wt%), while maintaining mechanically robust micro-architectures. Compared with other VP-based metal AM approaches, HIAM and HIAM-variant methods exhibit moderate shrinkage (20–70%), and nano-to-microscale feature resolution. It provides a unique balance among compositional flexibility, mechanical integrity, and scalability, making it particularly attractive for the fabrication of multifunctional metal micro-structures.

2.2.2 Infusion-reaction approaches and HIAM variants. Beyond the HIAM method, several variants have been developed to expand their capabilities. For example, similar infusion-reaction approaches have been used in conjunction with polymer-based 3D scaffold templates for direct metal ion infusion, eliminating the need for hydrogel transformation.[67,70,76] Some researchers reported the use of printed hydrogel as scaffold for direct metal ion infusion, eliminating the organogel to hydrogel transformation step.[68,69] These extensions broaden HIAM's applications, enabling the fabrication of functional components such as electrodes for water splitting or current collectors for batteries. Tiwari *et al.* reported the fabrication of 3D Cu/CuO_x/C transition catalysts with maximized active sites and improved mass transport for electrocatalytic water splitting.[76] Similarly, Martinez *et al.* demonstrated the fabrication of complex 3D-printed copper current collector structures with integrated loadbearing and energy storage functionalities.[67]

Several strategies have been proposed to address the weak interactions between hydrogel scaffolds and metal ions in HIAM, which limit ion loading capacity and can lead to defects such as cracks in the sintered structures. These approaches include complexation scaffold additive manufacturing,[72,73] ion-exchangeable hydrogel additive manufacturing,[71] and capillary force additive manufacturing.[74]

Complexation scaffold additive manufacturing utilizes surface complexation, where coordination bonds are formed between metal ions and functional groups on the hydrogel. For example, printed hydrogels with abundant carboxyl groups can dissociate in aqueous metal salt solutions, forming negatively charged carboxylate ions that coordinate with metal ions through lone pair electrons on oxygen atoms. Two main types

Table 3 Comparison of reported VP-based HIAM and HIAM-variant methods for metal AM

Target material	VP technique	Resin composition	Product composition	Mechanical properties	Feature dimensions	Ref.
Copper *etc.*	DLP	**Monomers/oligomers:** poly(ethylene glycol) diacrylate **PIs:** 2-dimethylamino-2-(4-methyl-benzyl)-1-(4-morpholin-4-ylphenyl)-butan-1-one, bis[4-(dimethylamino)phenyl]methanone **UV blocker:** 1-(phenyldiazenyl)naphthalen-2-ol **MPs:** copper nitrate, nickel nitrate *etc.* **Solvents:** *N*,*N*-dimethylformamide	**Cu:** 93 wt% **CuNi:** 86wt%	**Hardness:** Cu = 1.81 ± 0.37 GPa CuNi = 2.15 ± 0.22 GPa	**Beam diameter:** ∼40 μm; **Shrinkage:** ∼60–70%	61
Copper	DLP	**Monomers/oligomers:** poly(ethylene glycol) diacrylate **PIs:** diphenyl(2,4,6-trimethyl benzoyl)phosphine oxide **MPs:** copper II nitrate hemipentahydrate **Solvents:** water	Not reported	**Compressive strength:** 19.39 MPa **Hardness:** 0.272 ± 0.039 GPa	**Shrinkage:** *X*–*Y* = 65% *Z* = 41%	67
Iron, copper *etc.*	DLP	**Monomers/oligomers:** poly(ethylene glycol) diacrylate **PIs:** lithium phenyl-2,4,6-trimethylbenzoylphosphinate **UV blockers:** tartrazine **MPs:** iron(III) chloride hexahydrate, iron(II) chloride tetrahydrate, copper(II) nitrate trihydrate *etc.* **Solvents:** water	Not reported	**Compressive strength:** Fe_2O_3 = 2 MPa Fe = ∼5 MPa **Hardness:** Fe = 1.75 ± 0.19 GPa Cu = 1.25 ± 0.16 GPa Ag = 1.21 ± 0.02 GPa **Elastic modulus:** Fe = 81 ± 6 GPa Cu = 53 ± 3 GPa Ag = 34 ± 1 GPa	**Shrinkage:** Fe_2O_3 = 20% Fe = 38% Cu = 46%	68
Iron oxide	VAM	**Monomers/oligomers:** poly(ethylene glycol) diacrylate **PIs:** DCPI 3001 **Radical scavengers:** 2,2,6,6-tetramethylpiperidin-1-yl)oxyl **MPs:** iron(III) chloride hexahydrate, iron(II) chloride tetrahydrate **Solvents:** dimethyl sulfoxide	Not reported	**Compressive strength:** 3.87 ± 0.39 MPa **Failure structural strain:** 0.16 ± 0.01	Not reported	69
Nickel, nickel oxide	TPL	**Monomers/oligomers:** poly(ethylene glycol) diacrylate **PIs:** 7-diethylamino-3-thenolcoumarin **MPs:** nickel nitrate hexahydrate **Solvents:** dimethyl sulfoxide, water	Not reported	**Yield strength:** ∼1–3 GPa at nanopillars diameter ≲ 300 nm	**Feature resolution:** 100 nm	70
Copper	DLP	**Monomers/oligomers:** poly(ethylene glycol) diacrylate, sodium acrylate **PIs:** PEG-BAPO **UV blockers:** tartrazine **Toughening agent:** cellulose nanocrystals **MPs:** copper sulfate **Solvents:** water	**Cu:** 96.2 wt%	**Compressive strength:** 10.3 MPa **Hardness:** 1.72 ± 0.22 GPa **Resistivity:** 4.91 μΩ cm	**Feature resolution:** ∼40 μm **Shrinkage:** 60%	71
Nickel cobalt alloy *etc.*	TPL	**Monomers/oligomers:** acrylic acid, pentaerythritol tetraacrylate **PIs:** 4,4-bis(diethylamino)benzophenone **MPs:** nickel nitrate hexahydrate, cobalt nitrate hexahydrate *etc.* **Solvents:** polyvinyl pyrrolidone	**NiCo:** 95 wt%	**Compressive strength:** ∼30 MPa **Surface roughness:** 18.9 nm	**Beam diameter:** 220 nm **Shrinkage:** 30–50%	72
Iron	DLP	**Monomers/oligomers:** acrylic acid, *N*-isopropylacrylamide, *N*,*N*′-methylenebisacrylamide **PIs:** lithium phenyl-2,4,6-trimethylbenzoylphosphinate **UV blockers:** basic violet 8 **MPs:** ferric chloride **Solvents:** water	Not reported	**Elastic modulus:** 45.83 ± 1.29 GPa **Hardness:** 1.01 ± 0.15 GPa	**Shrinkage:** ∼55%	73

Table 3 (*continued*)

Target material	VP technique	Resin composition	Product composition	Mechanical properties	Feature dimensions	Ref.
Gold, iron oxide *etc.*	TPL	**Monomers/oligomers:** IPS photoresist **MPs:** gold nanoparticles, iron oxide *etc.* **Solvents:** water, polyvinyl pyrrolidone	Not reported	**Surface roughness:** 46.6 ± 3.9 nm	**Feature resolution:** ~100 nm	74
γ-Alumina	DLP	**Monomers/oligomers:** acrylic acid **PIs:** diphenyl(2,4,6-trimethyl benzoyl)phosphine oxide **UV blockers:** sulforhodamine B **Proton scavengers:** propylene oxide **MPs:** aluminum chloride hexahydrate **Solvents:** water, ethanol	Not reported	Not reported	**Feature resolution:** 6 ± 1 μm **Shrinkage:** 62%	75

of surface complexation occur at the hydrogel-water interface: inner-sphere and outer-sphere complexation.[77] Inner-sphere complexation refers to the direct bonding between the ligands and metal ions, while outer-sphere complexation involves a thin layer of water molecules between the metal ions and ligands. For many transition metals, inner-sphere complexation is less favorable entropically, and tends to occur at higher metal concentrations.[66] Solution pH is another important parameter that affects not only metal speciation but also the surface charge of hydrogels and the coordination behavior of functional groups. For example, increasing the pH leads to deprotonating of carboxyl groups into carboxylate anions, expanding the hydrogel and creating more coordination sites.[66] Therefore, identifying the optimal pH is crucial for maximizing metal adsorption capacity and enhancing structural integrity by promoting pore collapse, which helps preserve the morphology of the final metal/ceramic parts. Following sintering and reduction, metal-complexed scaffolds are converted into 3D metal or alloy nanoarchitectures. Using this approach, Han *et al.* demonstrated the fabrication of various metal-alloy nanoarchitectures, including metals (Ni, Fe, Co, Cr, Cu, Au, and Ag) and alloys (NiCo and NiCoCu) by incorporating metal ions into acrylic acid (AAc)-based polymer scaffolds, shown schematically in Fig. 7A.[72] They further investigated the complexation efficiency of different resin systems and showed that the AAc-based scaffold exhibits significantly higher complexation efficiency, enabling the formation of metal/alloy nanoarchitectures with exceptional shape fidelity and structural integrity. FTIR spectra of the AAc-based polymer revealed the largest red shift in absorption peaks associated with oxygen-containing functional groups, while XPS O 1s spectra confirmed the formation of new metal–oxygen bonds after complexation. Similarly, Sun *et al.* developed a technique to fabricate iron structures with three-level hierarchical porosity.[73] In this process, a poly(*N*-isopropylacrylamide-*co*-acrylic acid) hydrogel lattice is first printed and then lyophilized to form a 3D porous scaffold. Metal ions are then introduced into the scaffold to form Fe^{3+} coordination with carboxyl groups, followed by sintering and reduction.

Printed hydrogel structures in ion-exchangeable hydrogel additive manufacturing are immersed in metal precursor solutions to facilitate metal ion exchange. This reversible chemical reaction occurs between free mobile ions in the hydrogel and metal ions of like charge presenting in the precursor solution. Ion-exchangeable hydrogels can absorb metal ions by replacing exchangeable protons released from oxygen-containing groups such as hydroxyl, carboxyl, sulfonate, and amino moieties. The efficiency and capacity of metal ion adsorption by ion exchange mainly depend on the ionic radius of the target ions and the number of available exchangeable sites, which are determined by the surface chemistry of the hydrogel.[66] The ion-exchanged hydrogel is subsequently calcined and reduced to yield the desired metal structures. It is well recognized that the concentration of metal precursors, immersion temperature, and duration are crucial factors influencing the ion exchange process. Optimizing these conditions can accelerate ion exchange rates,

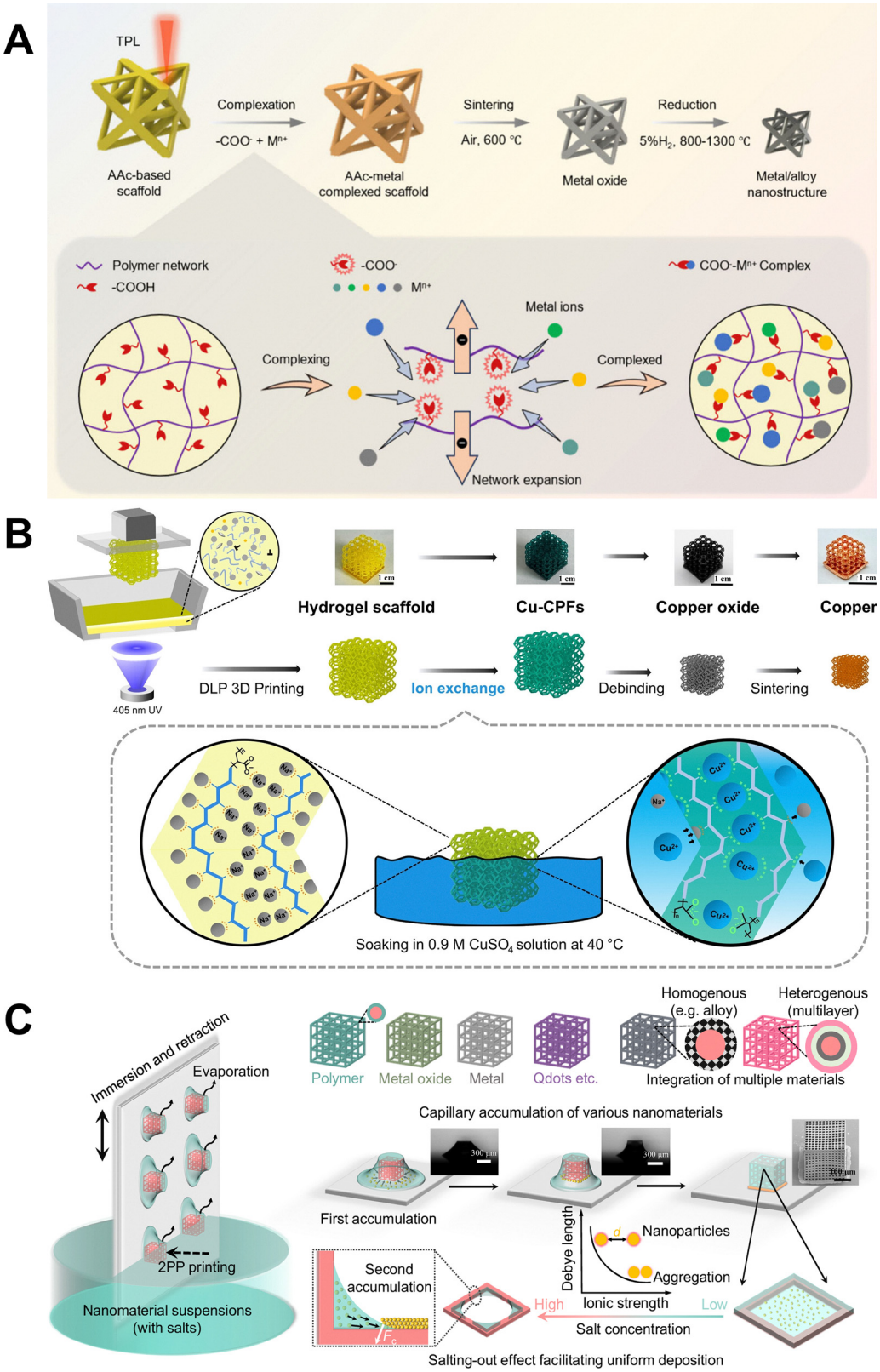

Fig. 7 Schematic illustrations of HIAM variants. (A) Schematic illustration of the complexation scaffold additive manufacturing of 3D metal/alloy nanoarchitectures and the complexation principle between metal ions and carboxyl groups within the polymer network. (B) Schematic of the ion-exchangeable hydrogel additive manufacturing of micro-architected copper that Na^+ ions in the hydrogel scaffolds are replaced by Cu^{2+} ions. (C) Schematic of the capillary force additive manufacturing of various nanomaterials, illustrating the key steps of capillary accumulation and deposition of nanomaterials. Adapted from ref. 71, 72 and 74 with permission.

enhance metal permeability, and ensure sufficient ion incorporation. Ma *et al.* reported the fabrication of ion-exchangeable hydrogels comprised of sodium acrylate as an ion-exchangeable monomer to produce complex and dense 3D micro-architected conductive copper structures (resistivity: 4.91 μΩ cm).[71] In this process, Na^+ ions in the hydrogel scaffolds are replaced by Cu^{2+} ions during soaking due to their strong coordination, shown schematically in Fig. 7B. Beyond metal AM, the ion-exchange approach is also widely used for removing pollutants such as heavy metal ions and organic dyes from water.[78]

Capillary force additive manufacturing utilizes non-specific physical interaction capillary force to adsorb metal nanoparticles onto 3D VP-printed polymer scaffolds, followed by sintering and reduction to produce 3D metallic architectures. These microscaffolds exhibit strong pinning capability at solid–liquid–gas three-phase interfaces, effectively trapping precursor solution within the scaffold and guiding the steady assembly of metal nanomaterials during evaporation, shown schematically in Fig. 7C. To ensure uniform and abundant nanomaterial deposition, the surface charge of metal nanoparticles is minimized *via* the salting out effect, reducing electrostatic repulsion. A representative example of this method is the work done by Lyu *et al.*, who reported the formation of 3D micro-/nanostructures composed of metal (*e.g.*, Au, Ag, Pt), and metal oxides (*e.g.*, Fe_3O_4, $BaTiO_3$) with high uniformity and nanoparticle mass loading on the microscaffold.[74]

Compared to heterogeneous and homogeneous resin approaches, the infusion-reaction approaches offer two key advantages. First, particle-free resins exhibit low viscosities and minimal light scattering, enabling high-resolution printing. Second, a wide range of commercially available metal salts can be used, allowing metal materials to be synthesized by simply dissolving metal salts or infusing metal nanoparticles in appropriate ratios after printing. While versatile and accessible, the utility of infusion-reaction approaches is limited by significant shrinkage during the polymer-to-metal/ceramic conversion process. This shrinkage often leads to low density, warping, cracking, and porosity in the final parts, negatively impacting their shape fidelity and structural integrity. Since shrinkage is inversely proportional to the amount of metal precursors in the organogel/hydrogel, recent research in this area has largely focused on the development of strategies that enhance precursor loading. Yee *et al.* used a repeated infusion-precipitation process where ammonia was used to chemically induce *in situ* formation of iron-oxide nanoparticles from infused precursors within a gel, followed by infusion of additional precursors to achieve high metal loadings, shown schematically in Fig. 8.[68,69] This approach enabled the fabrication of dense architected iron oxide and iron structures with conversion linear shrinkages of approximately 20% and 38% respectively.

3. Thermal decomposition of polymers in VP-based metal AM

Thermal decomposition of scaffolds is a critical step in VP-based metal AM processes, which typically involves two main stages: polymer degradation, and precursor conversion to target materials. A thorough understanding of these thermal decomposition mechanisms is essential for rational resin design and for optimizing both polymer processing and the synthesis of metal/ceramic components. Effective control of polymer decomposition requires insight into a variety of interrelated factors, including chemical reactions and property changes during heat treatment, as well as process parameters such as furnace ramp rates and atmosphere.

3.1 Chemical reactions during heat treatment

During thermal degradation of polymers, a series of chemical reactions occur through chain scission of macromolecules, which may proceed *via* radical, ionic, or mixed pathways. A typical multi-step free radical polymer degradation route is comprised of three steps: initiation, propagation and termination.[79] In the initiation step, free radicals are generated as the polymer backbone breaks into smaller fragments. This scission may occur either randomly within the main chain, at weak side groups, or at the chain ends. Chain-end degradation results in a high yield of monomers, while random scission primarily produces oligomers with only a small fraction of monomers. When oxygen is present, free radicals formed during initiation react with oxygen to produce highly reactive peroxide or hydroperoxide intermediates, which accelerate the degradation reactions.[79,80] In the propagation step, further chain scission could lead to volatile product formation, and adjacent degraded chains may undergo cross-linking reactions to form a char layer which can serve as a physical barrier to heat and oxygen, thereby slowing further decomposition.[81] The termination step involves free radical coupling or disproportionation, often resulting in byproducts such as ethers and carbonyl compounds. Volatile byproducts generated during polymer degradation can be identified in real time using mass spectroscopy and Fourier transform infrared spectrometry.

Alongside polymer degradation, a combination of polymer combustion and precursor decomposition, analogous to a solution combustion process, can occur in the condensed phase, gas phase, or mesophase.[82] Volatile intermediates serve as fuel, accumulating and mixing with oxygen in the furnace atmosphere. Upon reaching a critical ignition temperature, combustion begins, producing flue gases such as CO_2, H_2O, and NO_2. The heat generated from this exothermic combustion can lead to a self-propagating combustion reaction. Simultaneously, metal precursors embedded within the printed resin, for example in the form of crystallohydrates, undergo decomposition during heating. Common solutions used for solution combustion include metal nitrates (*e.g.*, $Cu(NO_3)_2$, $Ni(NO_3)_2$, $Al(NO_3)_3$) as oxidizers and organic fuels (*e.g.*, urea, citric acid, glycine).[83] If metal nitrates are used as precursors, this leads to the stepwise formation of low-water crystallohydrates, oxynitrates, and finally metal oxides.[84] Depending on the fuel-to-oxidizer ratio, solution combustion can proceed in three regimes: smoldering combustion synthesis, volume combustion synthesis, and self-propagating high-temperature synthesis.[85] A complexation analysis by Khaliullin *et al.* demonstrated that metal ions can alter the strength of internal

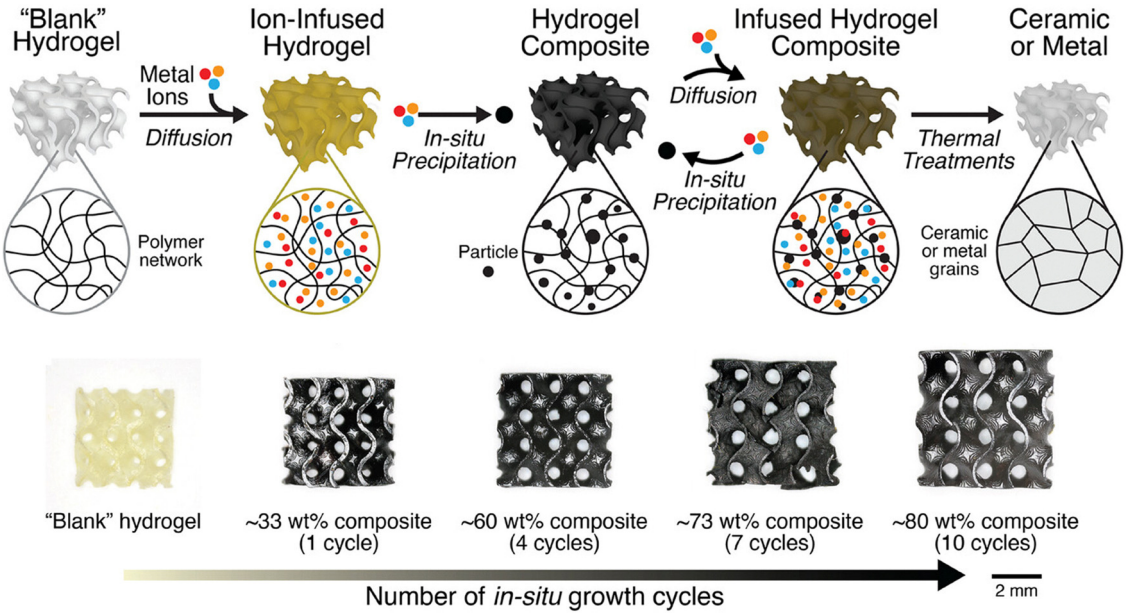

Fig. 8 Schematic of the hydrogel infusion and precipitation process for the VP of ceramics and metals. Adapted from ref. 68 with permission.

bonds in organic ligands by forming coordination complexes, and thus different fuel-to-oxidizer ratios can result in varying combustion temperatures.[84] Notably, when the fuel-to-oxidizer ratio equals one, the mixture does not require atmospheric oxygen for complete oxidation.[86] A representative reaction pathway for metal nitrates and glycine, as reported by Kumar *et al.*, includes the decomposition of glycine to yield NH_3, and of nitrates to form HNO_3, and metal oxides. NH_3 and HNO_3 then react exothermically to sustain combustion, generating hydrogen that further reduces the metal oxides to metallic products.[86]

To the best of our knowledge, no studies have quantitatively reported the fuel-to-oxidizer ratio in polymer-derived metal/ceramic synthesis process. Although the chemistry of combustion involves complex chain reactions, the calculation can be reasonably simplified under fuel/oxygen-rich conditions. In such cases, self-propagating high-temperature synthesis becomes the dominant mechanism, in which reactions follow a wave-like propagation through the medium.[85] It primarily includes four reactions: (1) complete oxidation of carbon to carbon dioxide, (2) complete oxidation of hydrogen to water, (3) complete oxidation of nitrogen to nitrogen oxides, and (4) complete formation of metal oxides.

3.2 Property changes during heat treatment

During thermal processing for VP-based metal AM, polymeric scaffolds undergo significant and irreversible changes in their physical and chemical properties. Analytical techniques such as thermogravimetry (TG) and differential scanning calorimetry (DSC) are widely employed to monitor property changes during the polymer decomposition process, which are correlated with the quality of the resulting metal/ceramic components. TG continuously measures the mass of a polymer sample as it is subjected to a controlled temperature program, tracking mass changes as a function of temperature and/or time. DSC measures the amount of heat adsorbed or released by a sample during heating, cooling, or isothermal hold. As the heating temperature approaches the decomposition point, decomposition reactions begin, and the glass transition temperature (T_g) of the polymer may change due to decreasing molecular weight and increasing formation of monomers.[79] In general, the decomposition begins at relatively low temperatures, particularly for hydrogels or other polymer matrices containing water. For example, around 100 °C, PEGda-based Cu ion infused hydrogels exhibit an early and sharp mass loss, indicated by the endothermic heat flow of approximately 0.25 W g^{-1} present in the DSC profiles, primarily due to the evaporation of excess water.[61,87] From approximately 100 °C to 500 °C, polymer gels often undergo a prolonged phase of mass loss, typically ending with a hold at certain temperature for sufficient time to ensure the total combustion of organic matrix.

The type of metal or ceramic precursors embedded within polymer scaffolds can significantly influence the thermal profile and final material quality.[88] For instance, nitrate salt-infused hydrogels show a sharp mass loss and a large exothermic event and at low temperatures (below 150 °C), generating large amounts of gas. The nitrated-derived gases are highly reactive and can further oxidize at elevated temperatures, promoting additional energetic reactions with the metal species.[89] These reactions can lead to the formation of open foamlike ceramic structures that are often crumbly and mechanically unstable. In contrast, Yaw *et al.* found that chloride salt-infused PEGda-based hydrogel systems with later decomposition events exhibit a smaller mass loss and a more moderate exothermic response, resulting in ceramic products of consistently higher quality.[64]

3.3 Heating processes and conditions

Post-process annealing plays a crucial role in enhancing the mechanical properties of parts produced *via* VP-based metal

AM by inducing changes in microstructure and crystallinity.[90] Structural shrinkage and deformation during annealing are governed by coupled thermal and diffusion processes, which are influenced by parameters, such as heating temperature, environmental pressure, surface-to-volume ratio, and cross-linking density.[91]

Due to the layer-by-layer fabrication process inherent to most AM methods and the nonuniform heat transfer between layers during photopolymerization, VP-based metal AM can develop uneven residual stress distributions within the fabricated parts, which leads to porosity manifested as voids, cracks, or inclusions, thereby reducing its mechanical properties, as shown in Fig. 9.[64,90] Annealing at high temperature helps mitigate these issues by relieving residual stresses and healing microstructural defects. When combined with high pressure, the process can force trapped gases out of the material, thereby eliminating porosity and leading to a denser and more uniform microstructure with improved fatigue and creep resistances.[92] Additionally, annealing promotes recrystallization, refining the grain structure and improving toughness and structural integrity of the printed parts. However, overheating or excessive exposure time to high temperatures can cause material microstructural coarsening or even melting, negatively impacting properties such as tensile strength.[93]

The atmosphere used during annealing is a crucial factor that influences the quality and performance of the final parts in VP-based metal AM. In addition to air, various process gases are commonly employed in heat treatment furnaces, including oxygen, hydrogen, nitrogen, helium, argon, carbon monoxide, carbon dioxide, ammonia, propane, methane, and butane. Among these, air and oxygen are the most reactive and are widely used in the fabrication of metal oxides. In contrast, inert or protective atmospheres such as those composed of nitrogen, helium, or argon are used to minimize undesired chemical reactions by providing a highly controlled environment. It has been reported that fewer cracks form in fabricated ceramics when the binder burnout is carried out in an inert atmosphere rather than in air, regardless of the heating rate.[94] This improvement is attributed to the reduction of internal gas pressure and the elimination of exothermic heat generated during binder oxidation.[95]

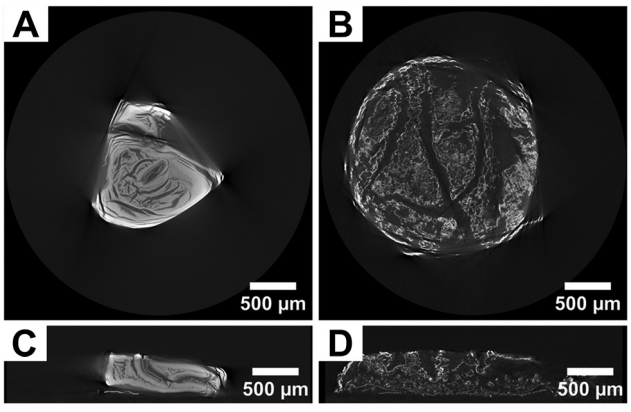

Fig. 9 X-ray computed tomography reconstruction slices of ceramics derived from gels infused with (A) $Cu(NO_3)_2$ and (B) $CuCl_2$, along with their corresponding vertical cross-sections (C) and (D), highlighting regions with large cracks and voids. Adapted from ref. 64 with permission.

Table 4 compares the target material, VP technique, and heating process and conditions of recently reported VP-based metal AM methods. As summarized in Table 4, the specific thermal processing approaches used vary based on resin type and target material. Ceramic systems generally require a two-step debinding and sintering process, while metal fabrication often involves a three-step debinding, sintering, and reduction sequence. From these studies, several practical design rules for achieving robust metallic structures can be identified. First, slow heating rates, typically less than 1 °C min^{-1} during debinding, are critical for minimizing internal gas evolution and crack formation. Second, the incorporation of intermediate isothermal holds, guided by TG data, particularly at temperatures corresponding to high mass loss rates, is essential for gradual polymer decomposition. Third, high sintering temperatures, typically 900–1600 °C, should be selected based on intrinsic material properties, including melting point, diffusion kinetics, and phase stability. Fourth, extended dwelling times, typically longer than 3 h, are important for achieving sufficient densification and maintaining structural integrity. Fifth, the processing atmosphere should be tailored to the desired product: oxidizing environments (*e.g.*, air) for oxide formation, and reducing atmospheres (*e.g.*, 5% H_2) for the production of pure metals or alloys, as discussed previously.

The pyrolysis behavior of polymeric materials during conversion to disordered carbon materials has been extensively investigated, and while the target material is different, insights from these systems are relevant to polymer-derived inorganic materials, since in some cases, disordered carbon exists as an intermediate. Specifically, the thermal decomposition pathways and residual carbon structure established during pyrolysis govern the chemical environment and microstructural template for subsequent annealing, where metal salts or oxides are reduced and crystallized into metallic architectures. A systematic investigation into the structural evolution of 3D-printed nanoarchitectures during isothermal pyrolysis in vacuum and inert atmosphere was conducted by Sun *et al.*[91] Analysis of pyrolysis-induced size reduction revealed that shrinkage occurred more rapidly with increasing temperatures (450, 500, and 550 °C), decreasing partial pressures (from 3 to $\sim 10^{-5}$ mbar), and higher surface-to-volume ratios. The results indicate that the effective activation energy for pyrolysis-induced morphological shrinkage is approximately four times higher under vacuum conditions than under a nitrogen atmosphere. Cross-sectional microstructural analysis further revealed oxygen accumulation at the edges of samples pyrolyzed under low vacuum, supporting the hypothesis that second-order reactions govern the desorption of volatile gases, primarily CO and CO_2, thereby lowering the effective activation energy during low-vacuum heating.

Table 4 Comparison of heating process and conditions of VP-based metal AM methods

Method	Target material	VP technique	Heating process and conditions	Ref.
Heterogeneous resin methods	Alumina	DLP	**Debinding:** ~0.9 °C min^{-1} to 600 °C for ~200 min under vacuum, then reheated at ~4 °C min^{-1} to 1000 °C for ~60 min under air[a] **Sintering:** 5 °C min^{-1} to 1650 °C for 2 h under air[a]	35
	Alumina	DLP	**Debinding:** 0.2 °C min^{-1} to 600 °C under N_2 **Sintering:** 1600 °C for 2 h	39
	Alumina	DLP	**Debinding:** 1 °C min^{-1} to 600 °C for 2 h under N_2[a] **Sintering:** Not reported	43
	Aluminum alloy	DLP	**Debinding:** 1 °C min^{-1} to 450 °C for 2 h under Ar **Sintering:** 10 °C min^{-1} to 600 °C for 2 h under Ar	44
	Zirconia	DLP	**Debinding:** 0.2 °C min^{-1} to 500 °C for 30 min under vacuum[a] **Sintering:** ~5 °C min^{-1} to 1600 °C for 2 h under vacuum	45
	Zirconia	SLA	**Debinding:** 0.1 °C min^{-1} to 530 °C under air **Sintering:** 2 °C min^{-1} to 1200 °C for 30 min under air	46
	Zirconia	DLP	**Debinding:** 0.5 °C min^{-1} to 450 °C for 1 h[a] **Sintering:** 3 °C min^{-1} to 1500 °C for 2 h[a]	37
	Copper	CLIP	**Debinding:** 1 °C min^{-1} to 600 °C for ~2 h under N_2[a] **Sintering:** 3 °C min^{-1} to 1000 °C for ~3 h under air[a] **Reduction:** 3 °C min^{-1} to 800 °C for 10 h under 5% H_2/Ar	36
	Copper	CLIP	**Debinding:** 1 °C min^{-1} to 600 °C for 2 h under N_2[a] **Sintering:** 1 °C min^{-1} to 1000 °C for 5 h under air[a] **Reduction:** 3 °C min^{-1} to 800 °C for 10 h under 5% H_2/Ar	47
	WC–Co hardmetals	SLA	**Debinding:** 5 °C min^{-1} to 850 °C for 40 min under H_2 or N_2[a] **Sintering:** 2.5 °C min^{-1} to 1440 °C for 2 h under vacuum[a]	48
Homogeneous resin methods	Zinc oxide	TPL	**Sintering:** 0.5 °C min^{-1} to 500 °C under air	49
	Platinum	TPL	**Sintering:** 1 °C min^{-1} to 600 °C for 1 h	51
	Tungsten, tungsten carbide	TPL	**Sintering:** 1 °C min^{-1} to 600 °C for 2 h[a] **Reduction:** 3 °C min^{-1} to 900 °C for 3 h under 5% H_2/Ar[a] **Carbothermal reduction:** 3 °C min^{-1} to 1000 °C for 3 h under 5% H_2/Ar	52
	Tungsten	DLP	**Debinding:** 1 °C min^{-1} to 600 °C for ~200 min under Ar, then reheated at 0.5 °C min^{-1} to 600 °C for ~120 min under air[a] **Sintering:** ~2 °C min^{-1} to 1200 °C for 5 h under 10% H_2/Ar[a]	53
	Nickel	TPL	**Debinding:** 2 °C min^{-1} to 1000 °C for 1 h under Ar **Sintering:** 2 °C min^{-1} to 600 °C for 1 h under 5% H_2/Ar	55
	Zr/Ti/SiOC	DLP	**Sintering:** 2 °C min^{-1} to 1200 °C for 1 h under N_2	56
	Ni/SiOC	Masked-SLA	**Sintering:** 1 °C min^{-1} to 600 °C for 2 h under Ar[a]	57
	Al/SiOC	DLP	**Debinding:** 1 °C min^{-1} to 900 °C for 2 h under Ar **Sintering:** 5 °C min^{-1} to 1100 °C for 2 h under air	58
	Copper *etc.*	DLP	**Sintering:** 0.25 °C min^{-1} to 700 °C for 3 h under air **Reduction:** 3 °C min^{-1} to 900 °C for 6 h under 5% H_2/Ar	61
HIAM and HIAM variants	Copper	DLP	**Debinding:** 0.2 °C min^{-1} to 450 °C for 2 h under air[a] **Sintering:** 2 °C min^{-1} to 750 °C for 6 h under air **Reduction:** 4 °C min^{-1} to 900 °C for 5 h under 5% H_2/Ar	67
	Iron, copper *etc.*	DLP	**Debinding:** 2 °C min^{-1} to 1000 °C for 30 min under N_2[a] **Sintering:** 2 °C min^{-1} to 1000 °C for 30 min under air[a] **Reduction:** under 5% H_2/N_2	68
	Nickel, nickel oxide	TPL	**Sintering:** 1 °C min^{-1} to 500 °C under air **Reduction:** 3 °C min^{-1} to 590 °C for 3 min under 5% H_2/N_2	70
	Copper	DLP	**Sintering:** 0.5 °C min^{-1} to 420 °C for 200 min under air[a] **Reduction:** 3 °C min^{-1} to 900 °C for 1000 min under 10% H_2/Ar[a]	71
	Nickel cobalt alloy *etc.*	TPL	**Sintering:** 1 °C min^{-1} to 600 °C for 2 h under air[a] **Reduction:** 2 °C min^{-1} to 800 °C under 5% H_2/N_2	72
	Iron	DLP	**Sintering:** 5 °C min^{-1} to 1500 °C for 1 h under air[a] **Reduction:** 5 °C min^{-1} to 900 °C for 3 h under 10% H_2/Ar	73
	Gold, iron oxide *etc.*	TPL	**Sintering:** 2 °C min^{-1} to 600 °C for 2 h under air	74
	γ-Alumina	DLP	**Sintering:** 1 °C min^{-1} to 850 °C for 2 h under air[a]	75

[a] Heating profile involves stepwise heating with several intermediate isothermal hold, which are not individually specified in the table.

4. Challenges and opportunities for VP-based metal AM

VP-based metal AM offers several advantages over conventional and other metal AM processes, including high precision, high resolution, rapid printing speed, and the ability to fabricate complex internal and external geometries. However, several challenges remain, which must be addressed in future research.

4.1 Multimaterials and high-entropy alloys

Metallic multimaterials, which incorporate different metallic constituents together within one object, exhibit a wide range of unique mechanical, electrical, chemical, and optical properties.[96] These characteristics make them highly promising for applications such as batteries, turbine blades, soft robotics, and flexible sensors.[97,98] However, their widespread implementation remains constrained due to the lack of advanced

fabrication techniques capable of constructing well-designed 3D microarchitectures with coded material properties. VP-based metal AM offers a compelling solution as it eliminates the need for extensive assembly procedures such as gluing, aligning, fitting, and welding.[99] By integrating advanced hardware and programmable optical systems, VP techniques, such as material switching stereolithography, enable spatial control over the deposition of multiple metallic material during polymerization. This capability to fabricate metallic architectures with spatially varying mechanical properties is particularly attractive in contexts where conventional metallic multimaterial fabrication remains unattainable. However, they typically rely on manual or mechanical vat switching, or on dynamic fluid delivery within a single vat, which poses challenges due to hardware complexity, slower print speeds, cross-contamination, and significant material waste.[98] In contrast, dual-wavelength or multi-color printing, which employs photoresins with wavelength-selective behavior, presents a promising alternative for fabricating metallic multimaterials.[100,101] This approach enables spatially controlled polymerization of multiple material components within a single resin vat, simplifying hardware requirements while expanding design flexibility. It opens new opportunities for the fabrication of metallic multimaterials architectures with enhanced structural complexity, compositionally graded alloys, and programmable multifunctional materials.

A related class of materials that is of interest for VP-based processes is high-entropy alloys (HEAs), defined as alloys composed of four or more elements, typically in equimolar or nearly equimolar compositions that are stabilized by configurational mixing entropy.[102,103] HEAs have demonstrated superior mechanical and physical properties compared to traditional alloys, including outstanding specific strength, excellent high-temperature mechanical performance, exceptional ductility and fracture toughness at cryogenic temperatures, as well as superparamagnetism and superconductivity.[104] Recent innovations in HEAs have focused on developing novel alloy compositions or processing methods to tailor the microstructure and mechanical properties of bulk or monolithic components. However, only a small fraction of alloys in the vast number of possible HEAs compositions are likely to be practically useful. Identifying optimal compositions through conventional trial-and-error approach is resource-intensive, underscoring the need for high-throughput screening methods. VP-based metal AM methods, particularly those such as HIAM which rely on an infusion-reaction approach, present an attractive technique for fabricating HEAs because they require design and optimization of only a single photoresin composition, and enable facile compositional tuning during the infusion step. However, several fundamental challenges persist, such as limited understanding of mechanisms governing phase formation and phase stability in HEAs. Additionally, understanding the effects of interstitial elements, such as carbon, nitrogen, phosphorus, and oxygen on phase composition, microstructure, and mechanical properties of HEAs is essential for the successful implementation of VP-based AM of HEAs.

4.2 Future technological outlook

To address global environmental concerns, sustainable resin design using bio-based feedstocks has gained increasing attention. Feedstocks such as vegetable oils, polypeptides, and proteins offer chemical versatility and broad availability, providing a greener route to degradable, complex 3D network structures.[105–107] Beyond sustainable feedstocks, greener crosslinking chemistries are also needed, as current approaches largely rely on (meth)acrylation and epoxidation of bio-based feedstocks, limiting the formation of controlled network architectures. Moreover, conventional photoinitiators can be toxic to biological systems and the environment, prompting growing interest in photoinitiator-free polymerization strategies. For processes that make use of thermal polymer decomposition, there is opportunity to develop methods for recovering and valorizing pyrolysis byproducts in order to increase process efficiency.

In addition to advances in chemistry, the development and implementation of new processing strategies are essential to expand the capabilities of VP-based metal AM. A holistic understanding of mass transport and chemical transformation processes, supported by real-time characterization of conversion processes, will be important for understanding exactly what happens inside the ''black box'' of the furnace. As VP-based metal and ceramic AM transitions toward commercial-scale production, it must contend with the high throughput of conventional manufacturing methods such as injection molding. Many applications, such as architected energy materials, demand centimeter-scale devices with microscale feature resolution, a combination that remains challenging for VP due to the intrinsic trade-off between print resolution and build size. A high-throughput TPL approach recently reported by Gu *et al.* offers a promising pathway to overcome this limitation.[108] In this method, a metalens array produces more than 120 000 cooperative focal spots from a single incident beam, enabling simultaneous voxel writing while preserving the nanoscale resolution characteristic of TPL. Besides, a spatially adaptive illumination strategy compensates for optical nonuniformities to ensure consistent polymerization across the printing field. This approach enables parallel printing of replicated microstructures (more than 50 million microparticles per day) and centimeter-scale 3D architectures with feature sizes down to 113 nm.

5. Conclusion

VP-based additive manufacturing of metals and ceramics has emerged as a powerful platform for fabricating complex 3D functional materials with excellent geometric precision and design freedom. By combining digital light control, tailored photoresin chemistry, and post-polymerization thermal conversion, VP enables access to micro- and nano-architected metal and ceramic structures that are difficult or impossible to achieve using conventional manufacturing routes, with potential application spaces ranging from biomedical devices to energy materials

to aerospace components. Continued progress in VP-based additive manufacturing of metals and ceramics will require a combination of new materials synthesis pathways, expanding the range of post-processing conditions and modalities, and identifying applications that will maximally benefit from the geometric freedom and material selection available to these processes. Looking forward, we envision a future in which micro- and nano-scale objects formed from an unrestricted palette of inorganic materials can be fabricated with easily accessible tools and precursors, allowing VP-based AM of metals and ceramics to be a go-to tool for researchers across a wide breadth of fields.

Author contributions

Jie Zeng: writing the original manuscript, editing. Max A. Saccone: writing, editing, supervision, funding acquisition.

Conflicts of interest

There are no conflicts of interest to declare.

Data availability

This review article does not contain new data that have been generated or analyzed by the author. All of the data referenced in this paper are available in the original publications that are cited in the reference list.

Acknowledgements

The authors acknowledge financial support of this work by the University of Colorado Boulder.

References

1 A. Vafadar, F. Guzzomi, A. Rassau and K. Hayward, Advances in Metal Additive Manufacturing: A Review of Common Processes, Industrial Applications, and Current Challenges, *Appl. Sci.*, 2021, **11**(3), 1213, DOI: 10.3390/app11031213.
2 M. Armstrong, H. Mehrabi and N. Naveed, An Overview of Modern Metal Additive Manufacturing Technology, *J. Manuf. Process.*, 2022, **84**, 1001–1029, DOI: 10.1016/j.jmapro.2022.10.060.
3 A. Bandyopadhyay, Y. Zhang and S. Bose, Recent Developments in Metal Additive Manufacturing, *Curr. Opin. Chem. Eng.*, 2020, **28**, 96–104, DOI: 10.1016/j.coche.2020.03.001.
4 K. V. Wong and A. Hernandez, A Review of Additive Manufacturing, *ISRN Mech. Eng.*, 2012, **2012**, 1–10, DOI: 10.5402/2012/208760.
5 ASTM ISO/ASTM52900. *Standard Terminology for Additive Manufacturing Technologies*, 2017.
6 I. Gibson; D. Rosen; B. Stucker and M. Khorasani, *Additive Manufacturing Technologies*, Springer International Publishing, Cham, 2021, DOI: 10.1007/978-3-030-56127-7.
7 R. C, R. Shanmugam, M. Ramoni and G. Bk, A Review on Additive Manufacturing for Aerospace Application, *Mater. Res. Express*, 2024, **11**(2), 022001, DOI: 10.1088/2053-1591/ad21ad.
8 J. C. Vasco, Additive Manufacturing for the Automotive Industry, *Additive Manufacturing*, Elsevier, 2021, pp. 505–530, DOI: 10.1016/B978-0-12-818411-0.00010-0.
9 J. L. Amaya-Rivas, B. S. Perero, C. G. Helguero, J. L. Hurel, J. M. Peralta, F. A. Flores and J. D. Alvarado, Future Trends of Additive Manufacturing in Medical Applications: An Overview, *Heliyon*, 2024, **10**(5), e26641, DOI: 10.1016/j.heliyon.2024.e26641.
10 K. Aghaee, L. Li, A. Roshan and P. Namakiaraghi, Additive Manufacturing Evolution in Construction: From Individual Terrestrial to Collective, Aerial, and Extraterrestrial Applications, *J. Build. Eng.*, 2024, **96**, 110389, DOI: 10.1016/j.jobe.2024.110389.
11 J. Xu, Y. Fei, Y. Zhu, W. Yu, D. Yao and J. G. Zhou, A Review of Non-Powder-Bed Metal Additive Manufacturing: Techniques and Challenges, *Materials*, 2024, **17**(19), 4717, DOI: 10.3390/ma17194717.
12 H. Y. Ma, J. C. Wang, P. Qin, Y. J. Liu, L. Y. Chen, L. Q. Wang and L. C. Zhang, Advances in Additively Manufactured Titanium Alloys by Powder Bed Fusion and Directed Energy Deposition: Microstructure, Defects, and Mechanical Behavior, *J. Mater. Sci. Technol.*, 2024, **183**, 32–62, DOI: 10.1016/j.jmst.2023.11.003.
13 S. D. Jadhav, P. P. Dhekne, S. Dadbakhsh, J.-P. Kruth, J. Van Humbeeck and K. Vanmeensel, Surface Modified Copper Alloy Powder for Reliable Laser-Based Additive Manufacturing, *Addit. Manuf.*, 2020, **35**, 101418, DOI: 10.1016/j.addma.2020.101418.
14 Photopolymers Market (2025–2033) Size, Share & Trends Analysis Report By Performance (Low, Mid, High), By Technology (SLA, DLP, cDLP), By Application (Dental, Medical, Audiology, Jewellery), By Region and Segment Forecasts; GVR-4-68040-123-3, https://www.grandviewresearch.com/industry-analysis/photopolymers-marketreport.
15 W. Charles, Hull. Apparatus for Production of Three-Dimensional Objects by Stereolithography, 4575330.
16 J. R. Tumbleston, D. Shirvanyants, N. Ermoshkin, R. Janusziewicz, A. R. Johnson, D. Kelly, K. Chen, R. Pinschmidt, J. P. Rolland, A. Ermoshkin, E. T. Samulski and J. M. DeSimone, Continuous Liquid Interface Production of 3D Objects, *Science*, 2015, **347**(6228), 1349–1352, DOI: 10.1126/science.aaa2397.
17 W. Haske, V. W. Chen, J. M. Hales, W. Dong, S. Barlow, S. R. Marder and J. W. Perry, 65 Nm Feature Sizes Using Visible Wavelength 3-D Multiphoton Lithography, *Opt. Express*, 2007, **15**(6), 3426, DOI: 10.1364/OE.15.003426.
18 Z. Gan, Y. Cao, R. A. Evans and M. Gu, Three-Dimensional Deep Sub-Diffraction Optical Beam Lithography with 9 Nm Feature Size, *Nat. Commun.*, 2013, **4**(1), 2061, DOI: 10.1038/ncomms3061.
19 V. Harinarayana and Y. C. Shin, Two-Photon Lithography for Three-Dimensional Fabrication in Micro/Nanoscale

Regime: A Comprehensive Review, *Opt. Laser Technol.*, 2021, **142**, 107180, DOI: 10.1016/j.optlastec.2021.107180.

20 B. E. Kelly, I. Bhattacharya, H. Heidari, M. Shusteff, C. M. Spadaccini and H. K. Taylor, Volumetric Additive Manufacturing *via* Tomographic Reconstruction, *Science*, 2019, **363**(6431), 1075–1079, DOI: 10.1126/science.aau7114.

21 P. N. Bernal, S. Florczak, S. Inacker, X. Kuang, J. Madrid-Wolff, M. Regehly, S. Hecht, Y. S. Zhang, C. Moser and R. Levato, The Road Ahead in Materials and Technologies for Volumetric 3D Printing, *Nat. Rev. Mater.*, 2025, **10**, 826–841, DOI: 10.1038/s41578-025-00785-3.

22 G. Lipkowitz, M. A. Saccone, M. A. Panzer, I. A. Coates, K. Hsiao, D. Ilyn, J. M. Kronenfeld, J. R. Tumbleston, E. S. G. Shaqfeh and J. M. DeSimone, Growing Three-Dimensional Objects with Light, *Proc. Natl. Acad. Sci. U. S. A.*, 2024, **121**(28), e2303648121, DOI: 10.1073/pnas.2303648121.

23 X. He, L. Zang, Y. Xin and Y. Zou, An Overview of Photopolymerization and Its Diverse Applications, *Appl. Res.*, 2023, **2**(6), e202300030, DOI: 10.1002/appl.202300030.

24 A. Bagheri and J. Jin, Photopolymerization in 3D Printing, *ACS Appl. Polym. Mater.*, 2019, **1**(4), 593–611, DOI: 10.1021/acsapm.8b00165.

25 S. C. Ligon, R. Liska, J. Stampfl, M. Gurr and R. Mülhaupt, Polymers for 3D Printing and Customized Additive Manufacturing, *Chem. Rev.*, 2017, **117**(15), 10212–10290, DOI: 10.1021/acs.chemrev.7b00074.

26 M. B. A. Tamez and I. Taha, A Review of Additive Manufacturing Technologies and Markets for Thermosetting Resins and Their Potential for Carbon Fiber Integration, *Addit. Manuf.*, 2021, **37**, 101748, DOI: 10.1016/j.addma.2020.101748.

27 J. V. Crivello, The Discovery and Development of Onium Salt Cationic Photoinitiators, *J. Polym. Sci., Part A:Polym. Chem.*, 1999, **37**(23), 4241–4254, DOI: 10.1002/(SICI)1099-0518(19991201)37:23<4241::AID-POLA1>3.0.CO;2-R.

28 S. Zakeri, M. Vippola and E. Levänen, A Comprehensive Review of the Photopolymerization of Ceramic Resins Used in Stereolithography, *Addit. Manuf.*, 2020, **35**, 101177, DOI: 10.1016/j.addma.2020.101177.

29 K. Li and Z. Zhao, The Effect of the Surfactants on the Formulation of UV-Curable SLA Alumina Suspension, *Ceram. Int.*, 2017, **43**(6), 4761–4767, DOI: 10.1016/j.ceramint.2016.11.143.

30 K. Chung, N. S. Nenov, S. Park, S. Park and C.-J. Bae, Design of Optimal Organic Materials System for Ceramic Suspension-Based Additive Manufacturing, *Adv. Eng. Mater.*, 2019, **21**(10), 1900445, DOI: 10.1002/adem.201900445.

31 M. L. Griffith and J. W. Halloran, Scattering of Ultraviolet Radiation in Turbid Suspensions, *J. Appl. Phys.*, 1997, **81**(6), 2538–2546, DOI: 10.1063/1.364311.

32 J. Sun, J. Binner and J. Bai, Effect of Surface Treatment on the Dispersion of Nano Zirconia Particles in Non-Aqueous Suspensions for Stereolithography, *J. Eur. Ceram. Soc.*, 2019, **39**(4), 1660–1667, DOI: 10.1016/j.jeurceramsoc.2018.10.024.

33 J. Liu, J. Jean and C. Li, Dispersion of Nano-Sized γ-Alumina Powder in Non-Polar Solvents, *J. Am. Ceram. Soc.*, 2006, **89**(3), 882–887, DOI: 10.1111/j.1551-2916.2005.00858.x.

34 H. Xing, B. Zou, Q. Lai, C. Huang, Q. Chen, X. Fu and Z. Shi, Preparation and Characterization of UV Curable Al2O3 Suspensions Applying for Stereolithography 3D Printing Ceramic Microcomponent, *Powder Technol.*, 2018, **338**, 153–161, DOI: 10.1016/j.powtec.2018.07.023.

35 G. Nie, Y. Li, P. Sheng, F. Zuo, H. Wu, L. Liu, X. Deng, Y. Bao and S. Wu, Microstructure Refinement-Homogenization and Flexural Strength Improvement of Al2O3 Ceramics Fabricated by DLP-Stereolithography Integrated with Chemical Precipitation Coating Process, *J. Adv. Ceram.*, 2021, **10**(4), 790–808, DOI: 10.1007/s40145-021-0473-2.

36 D. Joralmon, J. Walling, A. Rai and X. Li, Optimized Dispersion of Inorganic Metal Salts in Photocurable Resins for High-Precision Continuous 3D Printing of Complex Metal Structures, *Int. J. Mach. Tools Manuf.*, 2025, **206**, 104259, DOI: 10.1016/j.ijmachtools.2025.104259.

37 P. Sokola, M. Kalina, J. Smilek, P. Ptáček, J. Krouská, D. Salamon and T. Spusta, Kinetic Stability and Rheological Properties of Photosensitive Zirconia Suspensions for DLP Printing, *Ceram. Int.*, 2023, **49**(11), 18502–18509, DOI: 10.1016/j.ceramint.2023.02.223.

38 I. Kim, S. Kim, A. Andreu, J.-H. Kim and Y.-J. Yoon, Influence of Dispersant Concentration toward Enhancing Printing Precision and Surface Quality of Vat Photopolymerization 3D Printed Ceramics, *Addit. Manuf.*, 2022, **52**, 102659, DOI: 10.1016/j.addma.2022.102659.

39 X. Chen, J. Sun, P. Cai, J. Huang, H. Liang, J. Yuan, S. Yu and J. Bai, Enhancing Precision in Ceramic Vat Photopolymerization 3D Printing through Dispersant Optimization, *Ceram. Int.*, 2024, **50**(22), 45114–45124, DOI: 10.1016/j.ceramint.2024.08.351.

40 G. L. Goh, S. Z. Han Lee, D. J. Seng Goh, G. D. Goh, E. Cheah and W. Y. Yeong, Printing 3D Metallic Structures through Reduction Processes: Principle, Approaches, and Applications, *Prog. Mater. Sci.*, 2025, 101610, DOI: 10.1016/j.pmatsci.2025.101610.

41 X. Gao, X. Chen, W. Wang, N. Li, J. Li and R. He, Vat Photopolymerization Additive Manufacturing of B4C/Al Composites, *Mater. Today Commun.*, 2025, **47**, 113160, DOI: 10.1016/j.mtcomm.2025.113160.

42 Diptanshu, G. Miao and C. Ma, Vat Photopolymerization 3D Printing of Ceramics: Effects of Fine Powder, *Manuf. Lett.*, 2019, **21**, 20–23, DOI: 10.1016/j.mfglet.2019.07.001.

43 J. Kim, Y. Choi, C. W. Gal, H. Park, S. Yoon and H. Yun, Effect of Dispersants on Structural Integrity of 3D Printed Ceramics, *Int. J. Appl. Ceram. Technol.*, 2022, **19**(2), 968–978, DOI: 10.1111/ijac.13965.

44 Y. Gan, M. Liu, D. Dai, W. Liu, C. Qiao, S. Bai, C. Peng, R. Wang, D. Wu, J. He and X. Wang, 3D Printing of Aluminum Alloys by Vat Photopolymerization Using Radical Inhibitors, *Adv. Eng. Mater.*, 2025, **27**(12), 2500058, DOI: 10.1002/adem.202500058.

45 Y. Yao, H. Cui, W. Wang, B. Xing and Z. Zhao, High Performance Dental Zirconia Ceramics Fabricated by Vat Photopolymerization Based on Aqueous Suspension, *J. Eur. Ceram. Soc.*, 2024, **44**(16), 116795, DOI: 10.1016/j.jeurceramsoc.2024.116795.

46 A. Jugan, S. Marinel, L. Le Pluart, T. Marie, R. Herbinet and C. Manière, Elaboration of Printable Nanopowder Zirconia Suspensions for Vat Photopolymerization, *J. Mater. Eng. Perform.*, 2025, **34**, 28824–28833, DOI: 10.1007/s11665-025-11338-8.

47 D. Joralmon, T. Tang, S. R. Prakash, H. Verma, S. Kim and X. Li, Continuous 3D Printing of Metal Structures Using Ultrafast Mask Video Projection Initiated Vat Photopolymerization, *Addit. Manuf.*, 2024, **89**, 104314, DOI: 10.1016/j.addma.2024.104314.

48 Z. Liu, Z. Liu, K. Zhou, Z. Chen, K. Shi, X. Wang, C. Peng, R. Wang, S. Magdassi, J. He and X. Wang, Vat Photopolymerization Additive Manufacturing of WC-Co Hardmetals Enabled by In Situ Polymerization-Induced Microencapsulation, *ACS Appl. Mater. Interfaces*, 2025, **17**(4), 7190–7200, DOI: 10.1021/acsami.4c20608.

49 D. W. Yee, M. L. Lifson, B. W. Edwards and J. R. Greer, Additive Manufacturing of 3D-Architected Multifunctional Metal Oxides, *Adv. Mater.*, 2019, **31**(33), 1901345, DOI: 10.1002/adma.201901345.

50 A. Vyatskikh, A. Kudo, S. Delalande and J. R. Greer, Additive Manufacturing of Polymer-Derived Titania for One-Step Solar Water Purification, *Mater. Today Commun.*, 2018, **15**, 288–293, DOI: 10.1016/j.mtcomm.2018.02.010.

51 M. Luitz, M. Lunzer, A. Goralczyk, M. Mader, S. Bhagwat, A. Warmbold, D. Helmer, F. Kotz and B. E. Rapp, High Resolution Patterning of an Organic–Inorganic Photoresin for the Fabrication of Platinum Microstructures, *Adv. Mater.*, 2021, **33**(37), 2101992, DOI: 10.1002/adma.202101992.

52 M. Luitz, D. Pellegrini, M. Von Holst, K. Seteiz, L. Gröner, M. Schleyer, M. Daub, A. Warmbold, Y. Thomann, R. Thomann, F. Kotz-Helmer and B. E. Rapp, High-Resolution Patterning of Organic–Inorganic Photoresins for Tungsten and Tungsten Carbide Microstructures, *Adv. Eng. Mater.*, 2023, **25**(13), 2201927, DOI: 10.1002/adem.202201927.

53 J. Cai, S. Ma, W. Yi and J. Wang, Fabrication of High-Density Microarchitected Tungsten via DLP 3D Printing, *Adv. Sci.*, 2024, **11**(39), 2405487, DOI: 10.1002/advs.202405487.

54 D. W. Yee, M. A. Citrin, Z. W. Taylor, M. A. Saccone, V. L. Tovmasyan and J. R. Greer, Hydrogel-Based Additive Manufacturing of Lithium Cobalt Oxide, *Adv. Mater. Technol.*, 2021, **6**(2), 2000791, DOI: 10.1002/admt.202000791.

55 A. Vyatskikh, S. Delalande, A. Kudo, X. Zhang, C. M. Portela and J. R. Greer, Additive Manufacturing of 3D Nano-Architected Metals, *Nat. Commun.*, 2018, **9**(1), 593, DOI: 10.1038/s41467-018-03071-9.

56 Y. Fu, G. Xu, Z. Chen, C. Liu, D. Wang and C. Lao, Multiple Metals Doped Polymer-Derived SiOC Ceramics for 3D Printing, *Ceram. Int.*, 2018, **44**(10), 11030–11038, DOI: 10.1016/j.ceramint.2018.03.075.

57 J. Essmeister, L. Schachtner, E. Szoldatits, S. Schwarz, A. Lichtenegger, B. Baumann, K. Föttinger and T. Konegger, Polymer-Derived Ni/SiOC Materials Structured by Vat-Based Photopolymerization with Catalytic Activity in CO2 Methanation, *Open Ceram.*, 2023, **14**, 100350, DOI: 10.1016/j.oceram.2023.100350.

58 T. Hu, L. Yao, H. Mei, M. Zhang, H. Liu, R. Li, L. Cheng and L. Zhang, Structure Designable Al-Doped SiOC Polymer-Derived Ceramic for Efficient Pressure and High-Temperature Difunctional Detection, *J. Eur. Ceram. Soc.*, 2025, **45**(2), 116923, DOI: 10.1016/j.jeurceramsoc.2024.116923.

59 M. Chen, M. Zhong and J. A. Johnson, Light-Controlled Radical Polymerization: Mechanisms, Methods, and Applications, *Chem. Rev.*, 2016, **116**(17), 10167–10211, DOI: 10.1021/acs.chemrev.5b00671.

60 V. Ferraro, C. R. Adam, A. Vranic and S. Bräse, Recent Advances of Transition Metal Complexes for Photopolymerization and 3D Printing under Visible Light, *Adv. Funct. Mater.*, 2024, **34**(20), 2302157, DOI: 10.1002/adfm.202302157.

61 M. A. Saccone, R. A. Gallivan, K. Narita, D. W. Yee and J. R. Greer, Additive Manufacturing of Micro-Architected Metals *via* Hydrogel Infusion, *Nature*, 2022, **612**(7941), 685–690, DOI: 10.1038/s41586-022-05433-2.

62 Y. Liu, J. Zhang, R. Niu, M. Bayat, Y. Zhou, Y. Yin, Q. Tan, S. Liu, J. H. Hattel, M. Li, X. Huang, J. Cairney, Y.-S. Chen, M. Easton, C. Hutchinson and M.-X. Zhang, Manufacturing of High Strength and High Conductivity Copper with Laser Powder Bed Fusion, *Nat. Commun.*, 2024, **15**(1), 1283, DOI: 10.1038/s41467-024-45732-y.

63 T. T. Tran, R. A. Gallivan and J. R. Greer, Multiscale Microstructural and Mechanical Characterization of Cu–Ni Binary Alloys Reduced During Hydrogel Infusion-Based Additive Manufacturing (HIAM), *Small*, 2025, e01320, DOI: 10.1002/smll.202501320.

64 N. S. Yaw, M. G. Ferrier, R. J. Griffiths, J. A. Hammons, A. J. Swift, S. A. Di Pietro, J.-B. Forien, B. C. Childs, A. A. Martin, K. S. Holliday, X. Guo and J. R. Jeffries, Precursor Design for Additive Manufacturing of Ceramics through Hydrogel Infusion, *Inorg. Chem. Front.*, 2025, **12**(8), 3055–3072, DOI: 10.1039/D5QI00139K.

65 F. V. Lavrentev, V. V. Shilovskikh, V. S. Alabusheva, V. Y. Yurova, A. A. Nikitina, S. A. Ulasevich and E. V. Skorb, Diffusion-Limited Processes in Hydrogels with Chosen Applications from Drug Delivery to Electronic Components, *Molecules*, 2023, **28**(15), 5931, DOI: 10.3390/molecules28155931.

66 M. A. H. Badsha, M. Khan, B. Wu, A. Kumar and I. M. C. Lo, Role of Surface Functional Groups of Hydrogels in Metal Adsorption: From Performance to Mechanism, *J. Hazard. Mater.*, 2021, **408**, 124463, DOI: 10.1016/j.jhazmat.2020.124463.

67 A. C. Martinez, A. Maurel, B. Yelamanchi, A. A. Talin, S. Grugeon, S. Panier, L. Dupont, A. Aranzola, E. Schiaffino, S. T. Sreenivasan, P. Cortes and E. MacDonald, Combining

3D Printing of Copper Current Collectors and Electrophoretic Deposition of Electrode Materials for Structural Lithium-Ion Batteries, *Adv. Manuf.*, 2025, **13**(2), 462–475, DOI: 10.1007/s40436-024-00514-z.

68 Y. Ji, Y. Hong, D. R. Bhandari and D. W. Yee, Hydrogel-Based Vat Photopolymerization of Ceramics and Metals with Low Shrinkages via Repeated Infusion Precipitation, *Adv. Mater.*, 2025, e04951, DOI: 10.1002/adma.202504951.

69 Y. Ji, E. Su and D. W. Yee, Volumetric Additive Manufacturing of Composites *via* Hydrogel Infusion, *ACS Mater. Lett.*, 2025, **7**(8), 2850–2857, DOI: 10.1021/acsmaterialslett.5c00407.

70 W. Zhang, Z. Li, R. Dang, T. T. Tran, R. A. Gallivan, H. Gao and J. R. Greer, Suppressed Size Effect in Nanopillars with Hierarchical Microstructures Enabled by Nanoscale Additive Manufacturing, *Nano Lett.*, 2023, **23**(17), 8162–8170, DOI: 10.1021/acs.nanolett.3c02309.

71 S. Ma, W. Bai, D. Xiong, G. Shan, Z. Zhao, W. Yi and J. Wang, Additive Manufacturing of Micro-Architected Copper Based on an Ion-Exchangeable Hydrogel, *Angew. Chem., Int. Ed.*, 2024, **63**(23), e202405135, DOI: 10.1002/anie.202405135.

72 C. Han, R. Li, M. Jiang, K. Huang, Y. Tao, D. Wang, G. Wang, J. Ni, Y. Hu, D. Wu, J. Chu and J. Li, 3D Printing of Metal and Alloy Nanoarchitectures through a Complexation-Driven Strategy, *Nano Lett.*, 2025, **25**(20), 8294–8302, DOI: 10.1021/acs.nanolett.5c01420.

73 Z. Sun, X. Ming, Z. Xu, Y. Xu, T. Xie and J. Wu, 3D Printing of Hierarchically Structured Metals/Alloys Based on Ion-Infused Porous Hydrogels, *Adv. Funct. Mater.*, 2025, **35**(13), 2418035, DOI: 10.1002/adfm.202418035.

74 X. Lyu, Z. Zheng, A. Shiva, M. Han, C. B. Dayan, M. Zhang and M. Sitti, Capillary Trapping of Various Nanomaterials on Additively Manufactured Scaffolds for 3D Micro-/Nanofabrication, *Nat. Commun.*, 2024, **15**(1), 6693, DOI: 10.1038/s41467-024-51086-2.

75 M. Y. Moshkovitz, D. Paz and S. Magdassi, 3D Printing Transparent γ-Alumina Porous Structures Based on Photopolymerizable Sol–Gel Inks, *Adv. Mater. Technol.*, 2023, **8**(23), 2300123, DOI: 10.1002/admt.202300123.

76 A. P. Tiwari, M. S. Rahman and W. J. Scheideler, 3D Printed Microlattices of Transition Metal/Metal Oxides for Highly Stable and Efficient Water Splitting, *Adv. Mater. Technol.*, 2024, **9**(13), 2400160, DOI: 10.1002/admt.202400160.

77 B. Wu, J. Wan, Y. Zhang, B. Pan and I. M. C. Lo, Selective Phosphate Removal from Water and Wastewater Using Sorption: Process Fundamentals and Removal Mechanisms, *Environ. Sci. Technol.*, 2020, **54**(1), 50–66, DOI: 10.1021/acs.est.9b05569.

78 H. Zhu, S. Chen and Y. Luo, Adsorption Mechanisms of Hydrogels for Heavy Metal and Organic Dyes Removal: A Short Review, *J. Agric. Food Res.*, 2023, **12**, 100552, DOI: 10.1016/j.jafr.2023.100552.

79 S. Ray and R. P. Cooney, Thermal Degradation of Polymer and Polymer Composites, *Handbook of Environmental Degradation of Materials*, Elsevier, 2018, pp. 185–206, DOI: 10.1016/b978-0-323-52472-8.00009-5.

80 K. Pielichowski; J. Njuguna and T. M. Majka, *Thermal Degradation of Polymeric Materials*, Elsevier, Amsterdam Kidlington, Oxford Cambridge, MA, 2nd edn, 2023.

81 S. L. Madorsky and S. Straus, Thermal Degradation of Polymers at High Temperatures, *J. Res. Natl. Bur. Stand., Sect. A*, 1959, **63**(3), 261–268, DOI: 10.6028/jres.063A.020.

82 J. Shen, J. Liang, X. Lin, H. Lin, J. Yu and S. Wang, The Flame-Retardant Mechanisms and Preparation of Polymer Composites and Their Potential Application in Construction Engineering, *Polymers*, 2021, **14**(1), 82, DOI: 10.3390/polym14010082.

83 A. Varma, A. S. Mukasyan, A. S. Rogachev and K. V. Manukyan, Solution Combustion Synthesis of Nanoscale Materials, *Chem. Rev.*, 2016, **116**(23), 14493–14586, DOI: 10.1021/acs.chemrev.6b00279.

84 Sh. M. Khaliullin, V. D. Zhuravlev, V. G. Bamburov, A. A. Khort, S. I. Roslyakov, G. V. Trusov and D. O. Moskovskikh, Effect of the Residual Water Content in Gels on Solution Combustion Synthesis Temperature, *J. Sol–Gel Sci. Technol.*, 2020, **93**(2), 251–261, DOI: 10.1007/s10971-019-05189-8.

85 A. S. Mukasyan, C. Costello, K. P. Sherlock, D. Lafarga and A. Varma, Perovskite Membranes by Aqueous Combustion Synthesis: Synthesis and Properties, *Sep. Purif. Technol.*, 2001, **25**(1–3), 117–126, DOI: 10.1016/S1383-5866(01)00096-X.

86 A. Kumar, E. E. Wolf and A. S. Mukasyan, Solution Combustion Synthesis of Metal Nanopowders: Copper and Copper/Nickel Alloys, *AIChE J.*, 2011, **57**(12), 3473–3479, DOI: 10.1002/aic.12537.

87 V. Gun'ko, I. Savina and S. Mikhalovsky, Properties of Water Bound in Hydrogels, *Gels*, 2017, **3**(4), 37, DOI: 10.3390/gels3040037.

88 *Handbook of Sol-Gel Science and Technology*, ed. L. Klein, M. Aparicio and A. Jitianu, Springer International Publishing, Cham, 2016, DOI: 10.1007/978-3-319-19454-7.

89 Z. Ding, W. Martens and R. L. Frost, Thermal Activation of Copper Nitrate, *J. Mater. Sci. Lett.*, 2002, **21**(18), 1415–1417, DOI: 10.1023/a:1019962632204.

90 A. Diniță, A. Neacșa, A. I. Portoacă, M. Tănase, C. N. Ilinca and I. N. Ramadan, Additive Manufacturing Post-Processing Treatments, a Review with Emphasis on Mechanical Characteristics, *Materials*, 2023, **16**(13), 4610, DOI: 10.3390/ma16134610.

91 Q. Sun, C. Dolle, C. Kurpiers, K. Kraft, M. Islam, R. Schwaiger, P. Gumbsch and Y. M. Eggeler, In Situ Pyrolysis of 3D Printed Building Blocks for Functional Nanoscale Metamaterials, *Adv. Funct. Mater.*, 2024, **34**(20), 2302358, DOI: 10.1002/adfm.202302358.

92 M. H. Bocanegra-Bernal, Hot Isostatic Pressing (HIP) Technology and Its Applications to Metals and Ceramics, *J. Mater. Sci.*, 2004, **39**(21), 6399–6420, DOI: 10.1023/B:JMSC.0000044878.11441.90.

93 O. O. Salman, C. Gammer, A. K. Chaubey, J. Eckert and S. Scudino, Effect of Heat Treatment on Microstructure and Mechanical Properties of 316L Steel Synthesized by Selective Laser Melting, *Mater. Sci. Eng., A*, 2019, **748**, 205–212, DOI: 10.1016/j.msea.2019.01.110.

94 J. Sun, J. Binner and J. Bai, 3D Printing of Zirconia via Digital Light Processing: Optimization of Slurry and Debinding Process, *J. Eur. Ceram. Soc.*, 2020, **40**(15), 5837–5844, DOI: 10.1016/j.jeurceramsoc.2020.05.079.

95 D. Komissarenko, S. Roland, B. S. M. Seeber, T. Graule and G. Blugan, DLP 3D Printing of High Strength Semi-Translucent Zirconia Ceramics with Relatively Low-Loaded UV-Curable Formulations, *Ceram. Int.*, 2023, **49**(12), 21008–21016, DOI: 10.1016/j.ceramint.2023.03.236.

96 D. Han and H. Lee, Recent Advances in Multi-Material Additive Manufacturing: Methods and Applications, *Curr. Opin. Chem. Eng.*, 2020, **28**, 158–166, DOI: 10.1016/j.coche.2020.03.004.

97 H. R. Vanaei, Multimaterial Additive Manufacturing of Metals and Alloys, *Multi-material Additive Manufacturing*, Elsevier, 2025, pp. 191–212, DOI: 10.1016/B978-0-443-29228-6.00009-8.

98 S. Subedi, S. Liu, W. Wang, S. M. A. Naser Shovon, X. Chen and H. O. T. Ware, Multi-Material Vat Photopolymerization 3D Printing: A Review of Mechanisms and Applications, *npj Adv. Manuf.*, 2024, **1**(1), 9, DOI: 10.1038/s44334-024-00005-w.

99 D. Chen and X. Zheng, Multi-Material Additive Manufacturing of Metamaterials with Giant, Tailorable Negative Poisson's Ratios, *Sci. Rep.*, 2018, **8**(1), 9139, DOI: 10.1038/s41598-018-26980-7.

100 K. C. H. Chin, G. Ovsepyan and A. J. Boydston, Multi-Color Dual Wavelength Vat Photopolymerization 3D Printing via Spatially Controlled Acidity, *Nat. Commun.*, 2024, **15**(1), 3867, DOI: 10.1038/s41467-024-48159-7.

101 S. G. Finnegan, A. M. Kinsey and A. J. Boydston, Selective Infusion of Spatially Controlled Domains via Vat Photopolymerization 3D-Printing for Chemically Diverse Multimaterial Parts, *Nat. Commun.*, 2025, **16**(1), 11258, DOI: 10.1038/s41467-025-66128-6.

102 J.-W. Yeh, Recent Progress in High-Entropy Alloys, *Ann. Chim. Sci. Mater.*, 2006, **31**(6), 633–648, DOI: 10.3166/acsm.31.633-648.

103 J.-W. Yeh, S.-K. Chen, S.-J. Lin, J.-Y. Gan, T.-S. Chin, T.-T. Shun, C.-H. Tsau and S.-Y. Chang, Nanostructured High-Entropy Alloys with Multiple Principal Elements: Novel Alloy Design Concepts and Outcomes, *Adv. Eng. Mater.*, 2004, **6**(5), 299–303, DOI: 10.1002/adem.200300567.

104 Y. F. Ye, Q. Wang, J. Lu, C. T. Liu and Y. Yang, High-Entropy Alloy: Challenges and Prospects, *Mater. Today*, 2016, **19**(6), 349–362, DOI: 10.1016/j.mattod.2015.11.026.

105 C.-U. Lee, S. J. Kim, R. B. Dietrich, A. L. Girard and A. J. Boydston, Additive Manufacturing *via* Protein Denaturation, *Green Chem.*, 2024, **26**(18), 9814–9822, DOI: 10.1039/D4GC02932A.

106 C. Vazquez-Martel, L. Becker, W. V. Liebig, P. Elsner and E. Blasco, Vegetable Oils as Sustainable Inks for Additive Manufacturing: A Comparative Study, *ACS Sustainable Chem. Eng.*, 2021, **9**(49), 16840–16848, DOI: 10.1021/acssuschemeng.1c06784.

107 R. D. Murphy, C. Delaney, S. Kolagatla, L. Florea, C. J. Hawker and A. Heise, Design of Statistical Copolypeptides as Multipurpose Hydrogel Resins in 3D Printing, *Adv. Funct. Mater.*, 2023, **33**(52), 2306710, DOI: 10.1002/adfm.202306710.

108 S. Gu, C. Mao, A. Guell Izard, S. Sadana, D. Terrel-Perez, M. Mettry-Yassa, W. Choi, W. Zhou, H. Yan, Z. Zhou, T. Massey, A. Abelson, Y. Zhou, S. Huang, C. Daraio, T. U. Tumkur, J. A. Fan and X. Xia, 3D Nanolithography with Metalens Arrays and Spatially Adaptive Illumination, *Nature*, 2025, **648**(8094), 591–599, DOI: 10.1038/s41586-025-09842-x.